Monthly Notices of the ROYAL ASTRONOMICAL SOCIETY

MNRAS **527,** 6675–6690 (2024) https://doi.org/10.1093/mnras/stad3508
Advance Access publication 2023 November 16

ExoMol line lists – LVI. The SO line list, MARVEL analysis of experimental transition data and refinement of the spectroscopic model

Ryan P. Brady,[1] Sergei N. Yurchenko,[1] Jonathan Tennyson[1★] and Gap-Sue Kim[2]

[1]*Department of Physics and Astronomy, University College London, Gower Street, WC1E 6BT London, UK*
[2]*Dharma College, Dongguk University, 30, Pildong-ro 1-gil, Jung-gu, Seoul 04620, Korea*

Accepted 2023 November 8. Received 2023 October 25; in original form 2023 September 8

ABSTRACT

A semi-empirical IR/Vis line list, SOLIS, for the sulphur monoxide molecule $^{32}S^{16}O$ is presented. SOLIS includes accurate empirical rovibrational energy levels, uncertainties, lifetimes, quantum number assignments, and transition probabilities in the form of Einstein A coefficients covering the $X\,^3\Sigma^-$, $a\,^1\Delta$, $b\,^1\Sigma^+$, $A\,^3\Pi$, $B\,^3\Sigma^-$, $A''\,^3\Sigma^+$, $A'\,^3\Delta$, and $e\,^1\Pi$ systems and wavenumber range up to 43 303.5 cm^{-1} ($\geq$230.93 nm) with $J \leq 69$. SOLIS has been computed by solving the rovibronic Schrödinger equation for diatomics using the general purpose variational code Duo and starting from a published *ab initio* spectroscopic model of SO (including potential energy curves, coupling curves, (transition) dipole moment curves) which is refined to experimental data. To this end, a database of 50 106 experimental transitions, 48 972 being non-redundant, has been compiled through the analysis of 29 experimental sources, and a self-consistent network of 8558 rovibronic energy levels for the X, a, b, A, B, and C electronic states has been generated with the MARVEL algorithm covering rotational and vibrational quantum numbers $J \leq 69$ and $v \leq 30$ and energies up to 52 350.40 cm^{-1}. No observed transitions connect to the $B\,^3\Sigma^-(v = 0)$ state which is required to model perturbations correctly, so we leave fitting the $B\,^3\Sigma^-$ and $C\,^3\Pi$ state UV model to a future project. The SO line list is available at ExoMol from www.exomol.com.

Key words: molecular data – planets and satellites: atmospheres – stars: atmospheres – exoplanets.

1 INTRODUCTION

Sulphur monoxide ($^{32}S^{16}O$) is an often transient diatomic molecule whose spectral properties are important for a wide range of environments. SO was first detected by radio astronomy in the interstellar medium by means of rotational spectroscopy and was the first $^3\Sigma$ ground state molecule to be detected in outer space (Gottlieb & Ball 1973). Additionally, SO was the first molecule observed using pure rotational transitions using microwave spectroscopy within its excited electronic states (Saito 1970). Since its first detection, SO has been observed in many astronomical environments, including the interstellar medium (Gottlieb et al. 1978), molecular clouds (Blake et al. 1987; Codella & Muders 1997), and planetary and lunar atmospheres (Na, Esposito & Skinner 1990; Lellouch 1996; de Pater et al. 2002; Belyaev et al. 2012). Numerous studies propose sulphur-bearing molecules, including SO, as constituents of volcanic planetary atmospheres (Zolotov & Fegley 1998; Krasnopolsky 2012; Hobbs et al. 2021). It also plays a role in many Solar system atmospheres, including that of Jupiter's moon Io (Lellouch 1996; de Pater et al. 2002) and of Venus (Na, Esposito & Skinner 1990; Belyaev et al. 2012), as well as Earth's own atmosphere (Burkholder et al. 1987). The recent detection of SO_2 in the atmosphere of WASP-39b (Rustamkulov et al. 2023) suggested SO as part of the photochemical production paths of SO_2 (Tsai et al. 2023). SO also has importance for (1) experimental applications in spectroscopy, such as UV lasing (Miller et al. 1991; Stuart, Cameron & Powell 1992); (2) astrophysical applications, such as shock modelling (Amin, Elnawawy & Elshalaby 1991; Chernin & Masson 1993; Bachiller 1996), magnetic field measurements in molecular clouds through observation of SO Zeemen splitting (Clark & Johnson 1974; Cazzoli et al. 2017), and studies into planetary formation mechanisms after its first detection within a protoplanetary disc (Pacheco-Vazquez et al. 2015), which supports sulphur-carrier based dust-formation channels (Vidal et al. 2017; Laas & Caselli 2019); (3) telluric applications, such as environmental studies of acid rain, since it is an intermediate in combustion reactions and has great chemical involvement with with N_2 and O_2 (Gaydon 1948; Burkholder et al. 1987).

The rovibrational structure of SO's spectrum for the $X\,^3\Sigma^-$ $a\,^1\Delta$, $b\,^1\Sigma^+$, $A\,^3\Pi$, and $B\,^3\Sigma^-$ electronic states at low vibrational excitation's has been studied by numerous works; we provide a full analysis of the experimental coverage on SO below. SO's electronic transitions were first reported by Martin (1932), and has since been subject to pure rotational (Yamamoto 1993; Klaus et al. 1994), electronic (Colin 1968, 1982; Setzer, Fink & Ramsay 1999), and rovibrational (Wong, Amano & Bernath 1982; Kanamori et al. 1985; Kanamori, Tiemann & Hirota 1988) spectroscopic studies. The pure rotational transitions within several vibrational states in the ground $X\,^3\Sigma^-$ electronic state have been measured in the terahertz (Klaus, Belov & Winnewisser 1997; Martin-Drumel et al. 2015), far-infrared (Clark & Delucia 1976; Cazzoli et al. 1994), and microwave regions (Lovas et al. 1992; Yamamoto 1993; Bogey et al. 1997). For

★ E-mail: j.tennyson@ucl.ac.uk

most of these spectra, SO was studied in non-local thermodynamic equilibrium (non-LTE) conditions, and so only relative intensities are available at best. Currently, there are no published absolute intensity measurements for SO. However, measurements of state lifetimes provide information on Einstein A coefficients and hence transition dipole moments (TDMs; Tennyson et al. 2016). Experimental lifetimes for the $b\,^1\Sigma^+$, $A\,^3\Pi$, and $B\,^3\Sigma^-$ states have been measured (Smith 1969; Elks & Western 1999; Yamasaki et al. 2003), and provide a valuable benchmark for our intensity calculations (see Section 5.1).

In this study, we present the largest compilation of experimental transition data and derived self-consistent empirical rovibrational energy levels for $^{32}S^{16}O$ to date. The derived energy levels where obtained through use of the MARVEL (Measured-Active-Rotational-Vibrational-Energy-Levels) spectroscopic network algorithm, to which we format the $^{32}S^{16}O$ data based on the MARVEL format (Furtenbacher, Császár & Tennyson 2007). We then refine our *ab initio* spectroscopic model (Brady et al. 2022) to our determined empirical energies to produce a hot semi-empirical line list SOLIS for $^{32}S^{16}O$ as part of the ExoMol project (Tennyson & Yurchenko 2012; Tennyson et al. 2020). The SOLIS line list supplements existing spectroscopic line list data for SO which are limited in coverage. For example, spectroscopic databases CDMS (Endres et al. 2016) and NIST (Kramida et al. 2020) databases contain data covering the microwave region only. HITRAN (Gordon et al. 2022) considers relatively low vibrational excitations for transitions between electronic states $X\,^3\Sigma^-$, $a\,^1\Delta$, and $b\,^1\Sigma^+$ only. We compare the SOLIS line list to the existing spectra data in Section 5.5.

2 THEORETICAL BACKGROUND

2.1 The MARVEL procedure

The critical evaluation of experimental transition data and formation of a self-consistent set of rovibronic energy levels is done through the MARVEL procedure (Furtenbacher, Császár & Tennyson 2007; Furtenbacher & Császár 2012a) which is built on the concept of spectroscopic networks (SN) (Császár & Furtenbacher 2011; Furtenbacher & Császár 2012b). Through a weighted linear least-squares protocol, MARVEL inverts the information contained within transition data to form a set of associated energy levels and uncertainties. Self consistency within the energy levels is then achieved through an iterative re-weighting algorithm which adjusts (increases) the uncertainties in the line positions to an optimized uncertainty $\sigma_{\rm opt}$ until they agree with the rest of the network.

The inverted MARVEL energy levels form nodes of a SN, which are linked by transitions, to which the validation of experimental information can be done on all data simultaneously using elements of network theory. The final energy level uncertainties in the SN are obtained through combining the optimal MARVEL uncertainties of all transitions connecting a given energy level. This study used a new implementation, MARVEL 4, which uses a bootstrap method to determine uncertainties in the empirical energy levels it determines (Tennyson et al. 2023). We used 100 iterations with the bootstrap method to determine the uncertainties in our empirical MARVEL energy levels.

2.2 Quantum numbers

We assign the rovibronic energy levels of $^{32}S^{16}O$ using the vibrational and rotational quantum numbers v and J, respectively, rotationless parity τ (*e*/*f*) and, in line with the Hund's case-(a) coupling scheme,

Table 1. Relation between the *e*/*f* and ± parities for linear molecules.

e/*f*	J	±
e	Even	+
e	Odd	−
f	Even	−
f	Odd	+

sublevels denoted by the fine structure F_{2S+1}. For $J \geq \Lambda + S$, the fine structure, F_{2S+1}, is defined for triplet electronic states via

$$\begin{aligned} F_1 &= N + S, \\ F_2 &= N, \\ F_3 &= N - S, \end{aligned} \tag{1}$$

where singlet states have no spin projection (i.e. F_2) and the total angular momentum excluding electronic and nuclear spin is labelled N. For linear molecules such as diatomics, levels with parity $+(-1)^J$ and $-(-1)^J$ are labelled e and f levels, respectively, and their relation to the ± parities are given in Table 1. We thus assign every experimental rovibrational transition using the v, J, *e*/*f*, F quantum numbers and standard spectroscopic notation for electronic states. For nuclear motion calculations, we use the quantum numbers Λ, Σ, and Ω to assign electronic states, which are the projection of orbital, spin, and total angular momentum on the bond axis, respectively, in addition to the state labels $X\,^3\Sigma^-$, $A\,^3\Pi$, $b\,^1\Sigma^+$, etc. For the $X\,^3\Sigma^-$ and $B\,^3\Sigma^-$ states, the spin-parity sub-levels in increasing energy order are

$$\begin{aligned} &(F_1, e): \Lambda = 0,\ \Sigma = 0,\ \Omega = 0, \\ &(F_2, f): \Lambda = 0,\ \Sigma = 1,\ \Omega = 1, \\ &(F_3, e): \Lambda = 0,\ \Sigma = 1,\ \Omega = 1, \end{aligned} \tag{2}$$

whereas for the regular $A\,^3\Pi$ state there is lambda-doubling (LD) and we have

$$\begin{aligned} &(F_1, e/f): \Lambda = 1,\ \Sigma = -1,\ \Omega = 0, \\ &(F_2, e/f): \Lambda = 1,\ \Sigma = \ \ 0,\ \Omega = 1, \\ &(F_3, e/f): \Lambda = 1,\ \Sigma = +1,\ \Omega = 2 \end{aligned} \tag{3}$$

and for the inverted $C\,^3\Pi$ state the sublevels increase in energy with decreasing Ω

$$\begin{aligned} &(F_1, e/f): \Lambda = 1,\ \Sigma = +1,\ \Omega = 2, \\ &(F_2, e/f): \Lambda = 1,\ \Sigma = \ \ 0,\ \Omega = 1, \\ &(F_3, e/f): \Lambda = 1,\ \Sigma = -1,\ \Omega = 0. \end{aligned} \tag{4}$$

Rigorous electric-dipole selection rules hold here, and can be summarized as

$$\begin{aligned} &+ \leftrightarrow -, \\ &\Delta J = \pm 1 (e \leftrightarrow e, f \rightarrow f), \\ &\Delta J = 0 (e \leftrightarrow f, 0 \not\leftrightarrow 0) \end{aligned}$$

3 THE EXPERIMENTAL TRANSITION DATABASE

3.1 Outline

Table 2 summarizes the experimental transition data included within our MARVEL analysis where each study is conveniently labelled with a tag including the first two digits of the year of publication and letters of the names of the first three authors in the form

Table 2. The experimental data sources included in the final MARVEL analysis and their spectroscopic coverage.

TAG	Source	Range (cm^{-1})	Electronic states	J	v	$\bar{\sigma}$ (cm^{-1})	V/T	Comm
64PoLi	Powell & Lide (1964)	0.435–2.2	*X-X*	0–3	0–0	1.07×10^{-5}	5/5	
64WiGoSa	Winnewisser et al. (1964)	2.87–5.74	*X-X*	1–4	0–0	1.67×10^{-5}	6/6	
69Colin	Colin (1969)	38672.94–39086.99	*A-X*	0–34	0–2	0.06	0/514	a,b,j
71BoMa	Bouchoux, Marchand & Janin (1971a)	11354.43–11606.78	*b-X*	5–96	0–2	0.40	154/227	a
72BoMa	Bouchoux & Marchand (1972)	12265.5–12625.29	*b-X*	8–32	0–4	0.40	123/165	a
74Tiemann	Tiemann (1974)	1.21–4.31	*X-X*	1–4	0–0	8.64×10^{-8}	6/6	
76ClDe	Clark & Delucia (1976)	4.26–11.6	*X-X*, *a-a*	0–9	0–0	4.50×10^{-5}	28/28	
82Colin	Colin (1982)	38255.26–39499.71	*A-X*	1–34	0–1	0.21	246/275	a,b
82WoAmBe	Wong, Amano & Bernath (1982)	3368.19–3386.30	*X-X*	1–9	0–3	2.00×10^{-3}	28/28	
82WuMoYe	Wu, Morgner & Yencha (1982)	23696.68–40816.33	*B-X*	0–0	1–19	2.00×10^{-4}	0/9	c
82Tiemann	Tiemann (1982)	1.21–9.89	*X-X*	1–9	0–0	3.53×10^{-5}	5/5	
85KaBuKa	Kanamori et al. (1985)	1041.95–1116.20	*X-X*	1–44	0–6	2.14×10^{-3}	50/94	c
86ClTe	Clyne & Tennyson (1986)	38051.24–38108.07	*A-X*	1–24	0–0	0.15	74/87	b
87BuLoHa	Burkholder et al. (1987)	1051.89–2296.98	*X-X*, *a-a*	0-47	0–2	1.64×10^{-3}	560/562	b,e
87EnKaHi	Endo, Kanamori & Hirota (1987)	10.9–12.8	*a-a*	7–9	0–5	9.00×10^{-7}	12/24	c
88KaTiHi	Kanamori, Tiemann & Hirota (1988)	1022.14-1121.26	*a-a*	2–41	0–5	2.01×10^{-3}	82/144	b,c,f
92LoSuOg	Lovas et al. (1992)	0.435–0.435	*X-X*	1–1	0–0	6.67×10^{-7}	0/1	
93Yamamoto	Yamamoto (1993)	2.8–15.4	*b-b*	1–11	0–8	5.89×10^{-7}	42/42	c
94CaClCo	Cazzoli et al. (1994)	19–62.8	*X-X*, *a-a*	9–45	0–0	1.46×10^{-4}	33/33	
94StCaPo	Stuart, Cameron & Powell (1994)	39619.44–40280.32	*A-X*, *B-X*	1–26	0–5	0.03	85/237	a,c
96KlSaBe	Klaus et al. (1996)	19.7–34.4	*X-X*	12–25	0–7	3.76×10^{-6}	45/71	c
97BoCiDe	Bogey et al. (1997)	11.7–31.2	*a-a*, *b-b*	8–22	0–13	1.40×10^{-6}	81/143	b,c
97KlBeWi	Klaus, Belov & Winnewisser (1997)	9.94–35.4	*a-a*, *b-b*	6–25	0-7	4.43×10^{-6}	41/55	c
99SeFiRa	Setzer, Fink & Ramsay (1999)	5792.97–10566.42	*a-X*, *b-X*	0–50	0-2	0.01	813/890	i
03KiYa	Kim & Yamamoto (2003)	1.11–2.8	*b-b*	0–2	0-22	6.67×10^{-8}	30/30	c
15MaHiMo	Martin-Drumel et al. (2015)	0.435–83.8	*X-X*	0–60	0-0	2.08×10^{-6}	110/110	d
17CaLaCo	Cazzoli et al. (2017)	2.87–28.1	*X-X*	0–20	0-0	6.67×10^{-5}	19/19	
CDMS	Endres et al. (2016)	0.43–125.40	*X-X*, *a-a*	0–69	0-1	3.97×10^{-2}	860/862	g
22HeStLy	Heays et al. (2022)	37856.62–52350.40	*A-X*, *B-X*, *C-X*	0-51	0-30	0.05	45434/45434	h

Notes. TAG denotes the identifier used to label the data sources throughout this paper, V/T describes the number of validated or included (V) data using the MARVEL procedure described in Section 2.1 relative to the total number of provided transitions (T), and the final column cross-references source specific comments (Comm) in Section 3.3.

'YYAaBbCc'. Table 2 includes the spectral coverage of each study, the associated quantum number coverage of their assignments, and the mean uncertainty of their results. We compiled a total of 50 106 transitions, of which 49 613 are non-redundant, from 29 experimental sources covering the $X\,^3\Sigma^-$, $a\,^1\Delta$, $b\,^1\Sigma^+$, $A\,^3\Pi$, $B\,^3\Sigma^-$, and $C\,^3\Pi$ electronic states of SO for rovibrational excitation's $J \leq 69$, $v \leq 30$.

3.2 General comments

A crucial limitation of the experimental data set for SO (Table 2) is in the vibrational state coverage of the lower electronic states. Transitions to/within states beyond the third vibrational excitation for $X\,^3\Sigma^-$, $a\,^1\Delta$, $b\,^1\Sigma^+$, and $A\,^3\Pi$ are severely lacking. Some vibrational transition data involving states beyond $v > 3$ are available, but inclusion of these within our MARVEL analysis often led to fragmented SNs.

Our literature review found that no transitions have been measured associated with the vibrational ground state of the $B\,^3\Sigma^-$ state, which makes it difficult to constrain its PEC minima during refinement of the spectroscopic model. The impact of this missing data is then amplified since the $B\,^3\Sigma^-$ and $C\,^3\Pi$ energies exhibit many mutual perturbations because of their overlapping potentials and strong coupling. To correctly model the perturbations one requires accurate positioning of the potentials corresponding to the resonating states relative to each other, which is made difficult because of the absence of data connecting to the $B\,^3\Sigma^-(v = 0)$ state.

Isotopologues of SO have been experimentally measured by several sources covering $^{33}S^{16}O$ (Klaus et al. 1996; Martin-Drumel et al. 2015; Heays et al. 2022), $^{34}S^{16}O$ (Tiemann 1974, 1982; Bogey, Demuynck & Destombes 1982; Burkholder et al. 1987; Yamamoto 1993; Klaus, Belov & Winnewisser 1997; Martin-Drumel et al. 2015; Heays et al. 2022), $^{32}S^{17}O$ (Klaus et al. 1996), $^{32}S^{18}O$ (Tiemann 1974; Bogey, Demuynck & Destombes 1982; Tiemann 1982; Burkholder et al. 1987; Klaus et al. 1996; Klaus, Belov & Winnewisser 1997) and the rare isotopologue $^{36}S^{16}O$ (Heays et al. 2022; Klaus et al. 1996). Few studies measure transitions within excited electronic states for these isotopologues, where Klaus, Belov & Winnewisser (1997) measured the $a\,^1\Delta$ and $b\,^1\Sigma^+$ states, Yamamoto (1993) measured the $b\,^1\Sigma^+$ state, and Heays et al. (2022) measured the higher $A\,^3\Pi$, $B\,^3\Sigma^-$, and $C\,^3\Pi$ electronic states. Low vibronic excitation is typically measured with similar J coverage as the main $^{32}S^{16}O$ isotopologue.

3.3 Source-specific comments

(a) A significant problem we faced during data analysis is that several literature sources did not provide obvious uncertainties on their line measurements, which is important for their validation within the MARVEL protocol (Section 2.1). We thus had to estimate their uncertainties through combination difference (CD) tests to other data in our database with known uncertainties where possible. These sources include Bouchoux, Marchand & Janin (1971a), Bouchoux & Marchand (1972), Colin (1969, 1982) and Stuart, Cameron & Powell

(1994). Initial uncertainties for these sources were assumed to be 0.05 cm^{-1} and manually increased with successive MARVEL runs until the data gave satisfactory CD relations with other sources. In the case of blended lines, their uncertainties were increased by a factor of $\sqrt{2}$ relative to the non-blended data which often resulted in their validation. As a result of this, the source uncertainties were estimated to be 0.02 cm^{-1} (Stuart, Cameron & Powell 1994), 0.4 cm^{-1} (Bouchoux, Marchand & Janin 1971b, 1972), 0.05 cm^{-1} (Colin 1969), and 0.2 cm^{-1} (Colin 1982).

(b) Another issue with the experimental transition data is the significant proportion of blended lines that are reported, such in the measurements by Colin (1969, 1982), Clyne & Tennyson (1986), Burkholder et al. (1987), Kanamori, Tiemann & Hirota (1988), and Bogey et al. (1997). To account for potential inaccuracy in their assignments the blended lines were given a lower weight in our SN model [see comment (a) above].

(c) The experimental sources Wu, Morgner & Yencha (1982), Kanamori et al. (1985), Endo, Kanamori & Hirota (1987), Kanamori, Tiemann & Hirota (1988), Yamamoto (1993), Stuart, Cameron & Powell (1994), Klaus et al. (1996), Bogey et al. (1997), Klaus, Belov & Winnewisser (1997) and Kim & Yamamoto (2003) provide transition data in high vibrational states which were removed from the MARVEL SN (see Section 3.2).

(d) 15MaHiMo (Martin-Drumel et al. 2015) provide much data on SO isotopologues with determined isotopically invariant parameters as well as other various constants for the lowest seven vibrational states.

(e) 87BuLoHa (Burkholder et al. 1987) contains a misprint in Table 1 column 5, the SO ($X\,^3\Sigma^-$, $v = 1 - 0$, $R(18)$) line should be 1108.81665 cm^{-1}, not 1008.81665 cm^{-1}.

(f) 88KaTiHi (Kanamori, Tiemann & Hirota 1988) provide 60 SO ($a\,^1\Delta$, $v = 3 - 4, 4 - 5$) transitions. If high vibrational data for SO becomes available these would be a prime source for inter-vibrational transition data to supplement our MARVEL dataset.

(g) A discrepancy in the CDMS data for the $X\,^3\Sigma^-$, $v = 1$ state of SO was found. The lowest $v = 1$ state energy had to be shifted by 26.4559 cm^{-1}. Furthermore, a shift of 6.478 cm^{-1} was found in the $a\,^1\Delta$, $v = 0$ CDMS data of SO, where the source of error may come from use of a high uncertainty $v = 0 - 0$ band centre due to Bielefeld et al. (1984). The relative energies between CDMS levels within the same vibrational levels are unaffected, hence the transition wavenumbers are correct, but were corrected before being used in analyses involving MARVEL.

(h) Heays et al. (2022) perform high-resolution FUV Fourier transform photoabsorption spectroscopy and provide the only published UV transition data covering the $C\,^3\Pi \leftarrow X\,^3\Sigma^-$ and $B\,^3\Sigma^-$ ($v = 4 \ldots 30$) $\leftarrow X\,^3\Sigma^-$ bands. Because of the large overlap and spin-orbit coupling (SOC) between the $B\,^3\Sigma^-$ and $C\,^3\Pi$ states, many perturbations are present within the experimental data which appear to be assigned accurately. They also provide transition data for the isotopologues $^{33}S^{16}O$ and $^{36}S^{16}O$.

(i) Setzer, Fink & Ramsay (1999) provide 74 $b\,^1\Sigma^+ - X\,^3\Sigma^-$ magnetic dipole transitions, which have the same selection rules as for electric dipole transitions except from the parity changing rule.

(j) We chose to omit the 540 $A\,^3\Pi\,(v' = 2) - X\,^3\Sigma^-\,(v'' = 0)$ transitions measured by Colin (1969) for two reasons: (1) they produced many conflicts with the more comprehensive and more accurate data by Heays et al. (2022); (2) use of MARVELized energies generated including these data for refining our spectroscopic model proved very difficult; we prescribed abnormalities in the energy structure to be due to the poor data which did not occur when using the equivalent MARVELized data from Heays et al. (2022).

3.4 MARVELization of the experimental transition data

The $^{32}S^{16}O$ spectroscopic network was built through input of 50 106 rovibronic transitions into MARVEL from the 29 data sources outlined in Table 2. 546 transitions were invalidated since their optimized uncertainties did not satisfy the validation condition $\sigma_{opt} - \sigma_{exp} < 0.05\,cm^{-1}$. Invalidation of transition data can be due to multiple reasons, errors in their quantum number assignment, in their measurement, in the digitization of their scanned data (especially in old papers), and simply because they are not self-consistent with the rest of the network. The latter is the most common cause of invalidation but since they usually connect few levels they are invalidated if the aforementioned reasons are not the cause. The invalidated transitions are removed from the MARVEL network but are kept in the MARVEL input file with a negative wavenumber transition frequency. We note the 590 transitions were excluded not because of invalidation through the MARVEL procedure and are detailed in comments *i* and *j* in Section 3.3.

The majority of transitions that were invalidated are for lines connecting $v > 3$ (69 per cent) because of the lack of inter-vibrational data energetically above $v > 3$ which, if included, resulted in the fragmentation of our central SN and the invalidation of otherwise seemingly reliable data sources. There are a lack of measurements of rotational transitions within these higher vibrational states. It was found that keeping data for $v \leq 3$ produced the largest set of self-consistent energy levels and hence SN. For $v \leq 3$, the experimental source that provided the most invalidated transitions is by Colin (1969) (44 per cent), who measured the only $A\,^3\Pi \rightarrow X\,^3\Sigma^-$ $v = 2 \rightarrow 0$ band transitions, which is important for the refinement of the $A\,^3\Pi$ potential energy curve (PEC). Colin (1969) measured $^{32}S^{16}O$ in emission by means of flash photolysis of sulphur-bearing gases using a medium-resolution quartz spectrograph. They provide no direct uncertainty on their line positions, but provide an uncertainty for their $X\,^3\Sigma^- \rightarrow B\,^3\Sigma^-$ bandheads of $\pm 1\,cm^{-1}$ obtained in their absorption study. If one uses this value as a metric for their line position uncertainties, then it is to be expected that data coming from Colin (1969) should be treated with caution, consequently leading to much of their data being invalidated. The majority of the remaining invalidated $v \leq 3$ data comes from Colin (1982) and Stuart, Cameron & Powell (1994) (21 and 22 per cent, respectively) who measure $X\,^3\Sigma^- \rightarrow A\,^3\Pi$ and $X\,^3\Sigma^- \rightarrow B\,^3\Sigma^-$ transition bands, respectively.

As a result of the critical evaluation of the experimental transition data, we invert and provide optimized uncertainties for 8558 rovibrational energy levels for $^{32}S^{16}O$ which forms a fully self-consistent SN. Fig. 1 plots the MARVEL energies versus the rotational quantum number J, where a large gap in the ~15 000–37 000 cm^{-1} region exists, corresponding to missing highly excited vibrational data in the $X\,^3\Sigma^-$, $a\,^1\Delta$, and $b\,^1\Sigma^+$ states and any experimental coverage of the intermediate electronic states $c\,^1\Sigma^-$, $A'\,^3\Delta$, and $A''\,^3\Sigma^+$. For the higher vibrational energy levels of each electronic state, there are also gaps in the rotational structure. The experimental transition frequencies collected as part of this work are provided in the Supporting Information to this paper in the MARVEL format alongside the resulting MARVEL empirical energy levels.

4 THE SPECTROSCOPIC MODEL

To produce the final semi-empirical line list for $^{32}S^{16}O$, we use the *ab initio* spectroscopic model presented in our recent work (Brady et al.

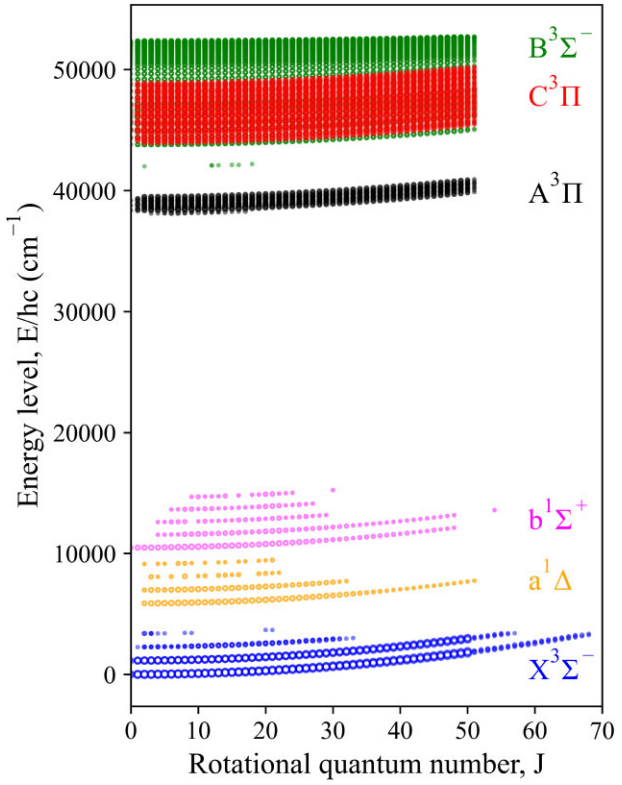

Figure 1. Our generated MARVEL energies plotted against the angular momentum quantum number J for the $X\,^3\Sigma^-$, $a\,^1\Delta$, $b\,^1\Sigma^+$, $A\,^3\Pi$, $B\,^3\Sigma^-$ and $C\,^3\Pi$ states. The vertical structure within each electronic state corresponds to the different vibrational levels. The size of the plot markers are directly proportional to the number of combination differences to that level in the SN.

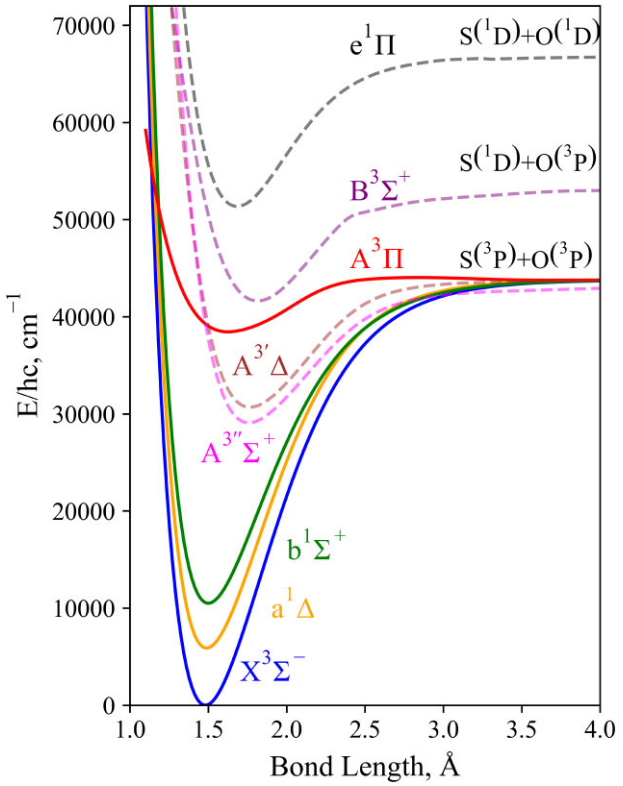

Figure 2. PECs of states included within our spectroscopic model of SO. The solid lines correspond to the potentials refined to MARVEL data, dashed lines correspond to states included within our model but have not been refined, where couplings to these states are essential for the accuracy of the $X\,^3\Sigma^-$, $a\,^1\Delta$, $b\,^1\Sigma^+$, and $A\,^3\Pi$ energies and band intensities.

2022) as a theoretical baseline for refinement to our MARVELized energy levels. Section 4.1 overviews the details of the *ab initio* model and Section 4.2 details the method used to refine it.

4.1 The *ab initio* spectrosopic model

The *ab initio* curves that make up our SO model (Brady et al. 2022) were computed using internally contracted multireference configuration interaction (ic-MRCI) level of theory and aug-cc-pV5Z basis sets. The active space and state averaging were chosen to have 12 active electrons with occupied (8, 3, 3, 0) and closed (4, 1, 1, 0) orbitals under C_{2v} symmetry. The model covers 13 electronic states: $X\,^3\Sigma^-$, $a\,^1\Delta$, $b\,^1\Sigma^+$, $c\,^1\Sigma^-$, $A''\,^3\Sigma^+$, $A'\,^3\Delta$, $A\,^3\Pi$, $B\,^3\Sigma^-$, $C\,^3\Pi$, $d\,^1\Pi$, $e\,^1\Pi$, $C'\,^3\Pi$, and $(3)^1\Pi$, which range up to 66 800 cm^{-1}, vastly beyond the scope of experimental coverage of the molecule. The *ab initio* model includes 13 PECs, 29 dipole and TDMs, 25 spin-orbit curves, and 18 electronic angular momentum curves on a grid of points over bond lengths 1–3 Å, where a diabatic representation was built by removing the avoided crossings between the spatially degenerate pairs $C\,^3\Pi$– $C'\,^3\Pi$ and $e\,^1\Pi$– $(3)^1\Pi$ through a property-based diabatization method.

4.2 Refinement

We refined our model to the IR/Vis region by fitting to the $X\,^3\Sigma^-$, $a\,^1\Delta$, $b\,^1\Sigma^+$, and $A\,^3\Pi$ energies only. We include the minimum number of states and couplings required such that our computed energies for these states agree with the MARVEL energies. Our refined model includes PECs and couplings connecting the $X\,^3\Sigma^-$, $a\,^1\Delta$, $b\,^1\Sigma^+$, $A\,^3\Pi$, $B\,^3\Sigma^{-\dagger}$, $A'\,^3\Delta^\dagger$, $A''\,^3\Sigma^{+\dagger}$, $e\,^1\Pi^\dagger$ states, see Fig. 2, where potentials for states labelled with a '†' superscript are not refined; these are included solely for their couplings within our model, but their dipoles are kept *ab initio*. These couplings, despite not being the dominant contributions to the energies of the $X\,^3\Sigma^-$, $a\,^1\Delta$, $b\,^1\Sigma^+$, and $A\,^3\Pi$ states, will redistribute intensities according to the intensity stealing mechanism (see Section 5 and the Appendix). First, we found that including the $c\,^1\Sigma^-$ and $d\,^1\Pi$ states within the model had negligible effect on the energies of the states of interest, and so they were omitted. Secondly, the inclusion of the $C\,^3\Pi$ state proved problematic and only worsened the fit. Because the $B\,^3\Sigma^-$ and $C\,^3\Pi$ PECs have large overlap and strong couplings between each other, their MARVEL energies include many perturbations because of resonances with each other, and also due to multiple avoided crossings with upper electronic states. Furthermore, due to the lack of important experimental data and consequent lack of proper constraint on the $B\,^3\Sigma^-$ PEC minimum, efforts to include the UV region within our fit proved too difficult to do satisfactorily. We therefore removed the $C\,^3\Pi$ state entirely from our model, but found including the $B\,^3\Sigma^-$, now without resonances with $C\,^3\Pi$, improved the fit of the $X\,^3\Sigma^-$, $a\,^1\Delta$, $b\,^1\Sigma^+$, and $A\,^3\Pi$ energies without being a major contribution to the accuracy of our model. Our initial efforts to fit the UV model constrained the $B\,^3\Sigma^-$ PEC enough such that expectation values of its couplings to other states in our model were sensible. Furthermore, the current need for the IR/Vis SO line list means we leave work on the UV model to a future study when the appropriate data becomes available.

Refinement of the *ab initio* model is facilitated through Duo, a general purpose variational (open access[1]) code that solves the rovibronic Schrödinger equation for diatomic molecules. A description of the methodologies used in Duo is given by Yurchenko et al. (2016). The refinement process goes as follows: (1) represent PECs, SOCs, EAMCs, DMCs, and other empirically fitted couplings such as rotational Born–Oppenheimer breakdown (BOB), spin–spin (SS), and spin-rotational (SR) curves with analytical forms; (2) compute energy levels using Duo through solving the rovibronic Schrödinger equation with curves defined; (3) fit parameters of the analytical functions such that the computed energy levels agree with the MARVEL energies.

Before refinement, the MARVEL energy level quantum number assignments need to be converted to the Duo quantum numbers J, τ, v, Λ, Σ, and Ω (see Section 2.2). Next, the i-th MARVEL energy was given a weight equal to

$$w_i = |\log_{10}(\sigma_i^{\rm opt})| \times n_i^{\rm CD}. \quad (5)$$

where $\sigma_i^{\rm opt}$ is its optimized uncertainty and $n_i^{\rm CD}$ is the number of combination differences/frequency of occurrence within the transition database. This weight is used in the Duo fit meaning energy levels with large uncertainty and a low number of combination differences will have less effect on the fit. Next, a running number must be defined to enumerate the global order of the energy levels calculated by Duo. These should agree with MARVEL's energy ordering for lower v and J numbers, but for higher energy states where Duo's calculated energies deviate significantly from the MARVEL data, the ordering of states between the two can differ. The running number we employ increases by 1 per vibrational excitation and by 100 per each electronic state, for example, the running numbers for $X\,^3\Sigma^-(v = 1)$ and $a\,^1\Delta(v = 2)$ are 1 and 102, respectively. This produced a sensible enumeration that effectively separated the energy levels and provided correct assignments of the calculated energy levels.

4.2.1 *Potential energy, spin-orbit, electronic angular momentum curves*

We represent all PECs using the Extended Morse Oscillator (EMO) function (Lee et al. 1999) which has the form

$$V(r) = V_{\rm e} + (A_{\rm e} - V_{\rm e})\left(1 - \exp\left[-\left(\sum_{i=0}^{N} a_i \xi_p(r)^i\right)(r - r_{\rm e})\right]\right)^2, \quad (6)$$

where $D_{\rm e} = A_{\rm e} - V_{\rm e}$ is the dissociation energy, $V_{\rm e}$ is the potential minimum and $A_{\rm e}$ is the asymptote, a_i are the expansion coefficients, $r_{\rm e}$ is the equilibrium bond length, and $\xi_p(r)$ is the so called Šurkus variable (Šurkus, Rakauskas & Bolotin 1984) given by

$$\xi_p(r) = \frac{r^p - r_{\rm e}^p}{r^p + r_{\rm e}^p} \quad (7)$$

with p as an integer parameter to allow for a better convergence at large bond lengths values. The $X\,^3\Sigma^-$, $a\,^1\Delta$, $b\,^1\Sigma^+$, $A\,^3\Pi$, $A'\,^3\Delta$, and $A''\,^3\Sigma^+$ states dissociate to the same asymptote $S(^3P) + O(^3P)$, which we initially set at 5.429 eV as reported by Huber & Herzberg (1979) and then floated during our fits, which converged to a nearby value of 5.42895 eV. The $B\,^3\Sigma^-$ state adiabatically correlates to $S(^1D) + O(^3P)$ which we set to a value of 6.5731 eV (53015.86 cm^{-1}) as determined through atomic energies from the NIST atomic database.

[1] github.com/Exomol

We shifted the PECs to the $X\,^3\Sigma^-$ minimum such that $V_{\rm e}(X\,^3\Sigma^-) = 0$ cm^{-1}. Since only the $X\,^3\Sigma^-$, $a\,^1\Delta$, $b\,^1\Sigma^+$, $A\,^3\Pi$, $B\,^3\Sigma^-$, and $C\,^3\Pi$ have experimental transition data to refine their PECs to, the *ab initio* PECs for the $A''\,^3\Sigma^+$, and $A'\,^3\Delta$ were fitted to the EMO function given in equation (6) using 10 expansion parameters which ensured accurate representation of their shape as given by *ab initio* calculations. Once we fitted the EMO functions, we could then tune their dissociation assymptotes to the 5.429 eV limit (Huber & Herzberg 1979). The $T_{\rm e}$ value for the $A''\,^3\Sigma^+$ state was fixed to 30 692 cm^{-1} as provided by Norwood & Ng (1989). We chose not to tune the $e\,^1\Pi$ *ab initio* PEC because it has a strong influence on the computed $X\,^3\Sigma^-$, $a\,^1\Delta$, $b\,^1\Sigma^+$, and $A\,^3\Pi$ energies and negatively effects our refinement when altering its potential. This negative effect is due to: (1) the shape of the PEC would be destroyed in tuning the $T_{\rm e}$ and $D_{\rm e}$ values; (2) the $e\,^1\Pi$ state has been diabatized (Brady et al. 2022), so tuning its PEC would change the avoided crossing morphology and hence a new diabatization of the spectroscopic model would be required; without experimental data covering $e\,^1\Pi$ we chose to keep the diabatized *ab initio* potential values.

In our refinement, the *ab initio* $B\,^3\Sigma^-$ PEC by Sarka & Nanbu (2019) was used instead of the PEC from our recent *ab initio* work (Brady et al. 2022). The latter did not employ sulphur-specific diffuse functions, which led to the underestimation of the $S(^3P) + O(^3P)$, $S(^1D) + O(^3P)$ and $S(^1D) + O(^1D)$ dissociation asymptotes and effected the $B\,^3\Sigma^-$ PEC the worst. The adiabatic character of the $B\,^3\Sigma^-$ PEC was modelled by diagonalizing a 2×2 matrix of diabatic potentials and the corresponding diabatic coupling which gives the adiabatic potential through solution of the quadratic equation for this system (Brady et al. 2022).

The *ab initio* SOCs and EAMCs were morphed from the grid representation to a Šurkus-like expansion (Prajapat et al. 2017; Yurchenko et al. 2018a) given by

$$F(r) = \sum_{i=0}^{N} B_i z^i(r)(r - \xi_p) + \xi_p B_\infty, \quad (8)$$

where B_i are the expansion coefficients, B_∞ is usually taken as zero in-order to allow the expansion to not diverge towards $r \to \infty$, and z is a damped displacement coordinate given by

$$z(r) = (r - r_{\rm e}) \exp[-\beta_2 (r - r_{\rm e})^2 - \beta_4 (r - r_{\rm e})^4], \quad (9)$$

where β_2 and β_4 are damping constants.

4.2.2 *Empirical rotational BOB, SS, and SR curves*

We fitted the phenomenological SS couplings and the empirical SR couplings of the triplet $X\,^3\Sigma^-$, $A\,^3\Pi$, and $B\,^3\Sigma^-$ states to account for additional Ω-splitting and to allow for additional variation of J, respectively, not described by the *ab initio* model (Kato 1993; Yurchenko et al. 2016). We also fitted rotational BOB curves for all but the $B\,^3\Sigma^-$ state to correct for the electron un-coupling to the nuclear motion producing an additional J^2 dependence in the residuals of the rovibronic energies and which can be thought of as a correction to the position-dependent rotational mass. Some SS, SR, and BOB couplings are modelled using equation (9) and some using a Šurkus polynomial expansion given by

$$F(r) = (1 - \xi_p) \sum_{i=0}^{N} a_i \xi_p^i + \xi_p a_\infty. \quad (10)$$

This greatly enhanced the accuracy of the finalized spectroscopic model.

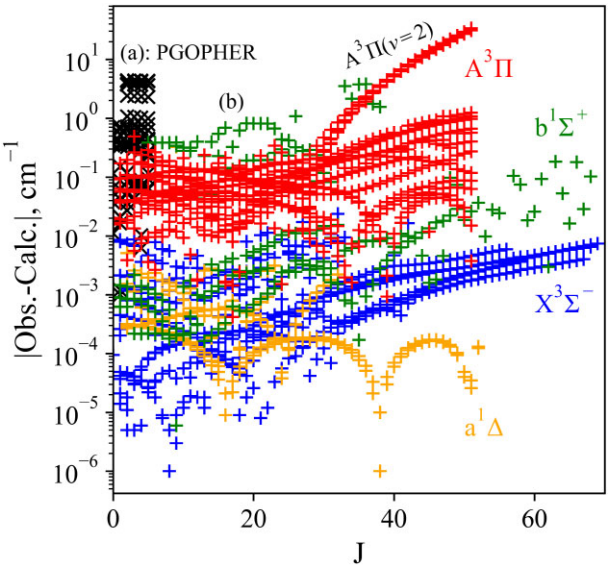

Figure 3. Visual representation of the difference between our MARVEL (Obs.) and the calculated (Calc.) energy levels as a function of J for the $X\,^3\Sigma^-$, $a\,^1\Delta$, $b\,^1\Sigma^+$, and $A\,^3\Pi$ states. (a) The Black crosses compare computed PGOPHER energies to our calculated Duo ones; (b) high scatter present in the MARVELized $b\,^1\Sigma^+(v = 3, 4)$ levels; ($A\,^3\Pi(v = 2)$) the Obs. – Calc. structure in the red points increases rapidly towards higher J's (see text).

4.3 Accuracy of the refined model

Fig. 3 illustrates the Observed minus Calculated (O – C) energy residuals as a function of the rotational quantum number J, and provides a metric on the accuracy of our model to reproduce our MARVELized energies. Most of the highly scattered energy levels have no combination differences with other sources, and so are effectively removed from the fit by setting their weight to 10^{-6}. We fit 100 per cent of 512 $X\,^3\Sigma^-$ ($J \leq 69$) energy levels with a total root-mean-square (rms) error of 3.13×10^{-3} cm^{-1}, 99 per cent of 244 $a\,^1\Delta$ ($J \leq 52$) energy levels with a rms error of 1.08×10^{-3} cm^{-1}, 95 per cent of 206 $b\,^1\Sigma^+$ ($J \leq 64$) energy levels with a total rms error of 0.27 cm^{-1}, and 78 per cent of 1262 $A\,^3\Pi$ ($J \leq 34$) energy levels with a rms error of 0.24 cm^{-1}. The above rms errors were calculated after filtering outliers from our data set which heavily influenced the rms, such as the scattered data of $b\,^1\Sigma^+(v = 3, 4)$, the $A\,^3\Pi(v = 2, J \geq 35)$ states, and a single data point of $a\,^1\Delta$. Elks & Western (1999) provide rotational constants for the $A\,^3\Pi$ ($v = 4 - 13$) states fitted to their $1 + 1$ resonance enhanced multiphoton ionization spectra which we used to compute low J ($J \leq 5$) energies via PGOPHER (Western 2017). These energies to our knowledge are the only ones covering the highly excited vibronic states of $A\,^3\Pi$ and so we use them to constrain the $A\,^3\Pi$ potential up to its dissociation. The black points in Fig. 3 for $J \leq 5$ [see label (a)] indicates the vibrational dependence in the residuals of these PGOPHER levels, which we manage to fit all within ∼4.5 cm^{-1}. Doing this allowed for a more physical description of the effective position-dependent correction to the rotational mass for the $A\,^3\Pi$ by constraining the potential gradient, and ultimately led to higher accuracy in the associated computed lifetimes (see Section 5.1).

Generally, the $b\,^1\Sigma^+$ data are of high quality and are reproduced by our model to within $\sim 10^{-4}$–10^{-3} cm^{-1} with the exception of high scatter within the MARVELized $b\,^1\Sigma^+(v = 3, 4)$ energies. This scatter can be seen in Fig. 3 around the label (b). One striking feature in Fig. 3 is of the $A\,^3\Pi$ ($v = 2$) Obs. – Calc. residuals, which, despite many attempts to model correctly, are poorly recovered in our model. We see a smooth, but rapid increase in the MARVEL energies with J of this band to ∼35 cm^{-1} at $J =$ 51. We postulate this is because a dark state pushes these energies upwards, some candidates being the $c\,^1\Sigma^-$, $A''\,^3\Sigma^+$, and $A'\,^3\Delta$ which cross through the $A\,^3\Pi$ potential, however, all attempts to correctly position their PECs relative to the $A\,^3\Pi$ failed to reproduce this behaviour. No published data on the crossing states exists, but it is entirely possible that a correct description of these electronic potentials could resolve this issue, and some empirical data could be used to constrain their curves better than blindly varying their positions.

Some residual J-dependence can be seen for the $X\,^3\Sigma^-$ and $b\,^1\Sigma^+$ states, where the former is due to J-dependent Ω-splitting and parity splitting within the $|\Omega| = 1$ levels, and the latter is due to vibrational dependence in the effective rotational centre not being fully accounted for. However, the residuals to the MARVEL energies are all $\leq 10^{-2}$ cm^{-1} which means the model should extrapolate well to higher J.

One major problem faced during the refinement was with the spin-orbit splitting of the $A\,^3\Pi$ energies, where experiment (Colin 1969, 1982) predicts regular Ω energy ordering, whereas multiple *ab initio* calculations reveal the $\langle A\,^3\Pi|\mathrm{SO}_z|A\,^3\Pi\rangle$ SOC to have a negative phase, suggesting irregular Ω energy ordering. Analysis by Colin (1969) shows the LD to be ∼1.2 cm^{-1} in the lowest energy Ω state with slight dependence on J, small doubling in the middle coupling which varies with $J(J + 1)$ and zero splitting for the highest component state. To choose whether we adopt the irregular Ω energy ordering suggested by *ab initio* calculations or the experimental assignment with a change in phase of the $\langle A\,^3\Pi|\mathrm{SO}_z|A\,^3\Pi\rangle$ SOC, we studied the *e/f* parity splitting of the $A\,^3\Pi$ energies since this would confirm what LD matrix elements to adopt. We saw that the slightly J-dependant ∼1.2 cm^{-1} parity splitting in the lowest energy state could only be resolved via the following LD element

$$\hat{\mathcal{H}}_{\mathrm{LD}} = \frac{1}{2}\alpha^{\mathrm{LD}}_{opq}(r)(\hat{S}^2_+ + \hat{S}^2_-) \tag{11}$$

with the LD constant being consistent with the Brown & Merer (1979) convention $\alpha^{\mathrm{LD}}_{opq} = o^{\mathrm{LD}} + p^{\mathrm{LD}} + q^{\mathrm{LD}}$ for a regular Ω energy ordering, i.e. the splitting is between states of $\Delta\Sigma = \pm 2$ which is only possible for a triplet state if $\Omega = 0$. If one adopted an irregular assignment scheme with $\Omega = 2$ for the lowest energy state, then one could not correctly model the J-dependence of the splitting since the element in equation (11) would be zero. We thus adopted the experimental assignment and changed the sign of our $\langle A\,^3\Pi|\mathrm{SO}_z|A\,^3\Pi\rangle$ SOC which should not break the phase consistency of the model since it is a diagonal coupling.

4.4 Dipole moment curves

We use the accurate *ab initio* ground state dipole moment function from Bernath, Johnson & Liévin (2022), who calculate with an ic-MRCI + Q level of theory including the Davidson corrections, scalar relativistic contributions using the exact 2-component (X2C) relativistic Hamiltonian, and aug-cc-pCV6Z-X2C basis sets. All other DMCs are computed at a level of theory described in Section 4.1. Within nuclear motion and intensity calculations, these dipoles are originally represented as a grid of *ab initio* points on the Duo defined grid, however, one sees a flattening of both the IR $X\,^3\Sigma^-$–$X\,^3\Sigma^-$ band spectrum and its variation of TDMC with vibrational excitation. The source of this non-physical flattening has been discussed by

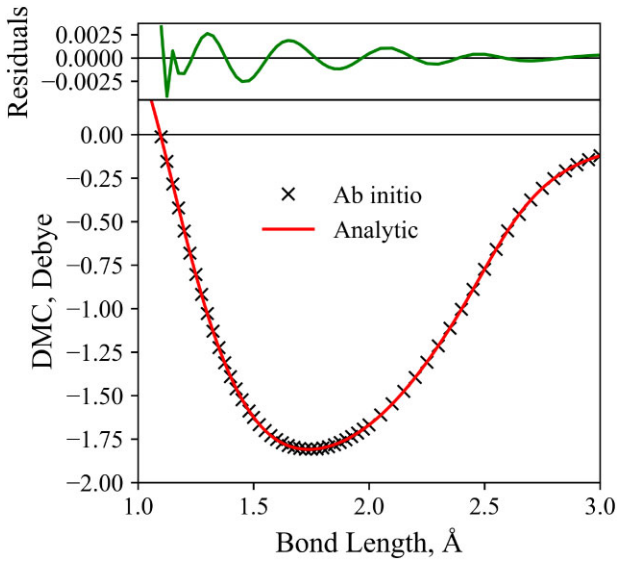

Figure 4. The *ab initio* $X\,^3\Sigma^-$ DMC provided by Bernath, Johnson & Liévin (2022), computed at an ic-MRCI + Q level of theory with full relativistic corrections using aug-cc-pCV6Z-X2C basis sets, is shown (black crosses) superimposed with our fitted analytical form using equation (12) (red line). The residuals to the *ab initio* DMC of our fit are shown in the top panel (green line).

Medvedev et al. (2015, 2016) and Medvedev & Ushakov (2022), who identify numerical noise as the culprit. This noise comes from DUO interpolating the given MOLPRO dipole grid points on to the DUO-defined grid. One can try to increase the precision of their transition moments from double to quadruple precision, but this seldom fixes the problem with any appreciable magnitude. The most effective method found is to represent the input dipole moments analytically. We chose to represent our $X\,^3\Sigma^-$ DMC using the 'irregular DMC' proposed in Medvedev & Ushakov (2022) which takes the form

$$\mathcal{D}_{\rm irreg}(r) = \chi(r; c_2, ..., c_6) \sum_{i=0}^{6} b_i T_i(z(r)), \tag{12}$$

where T_i are Chebyshev polynomials of the first kind, b_i are summation coefficients to be fit, $z(r)$ is a reduced variable in bond length similar to the damped polynomial coordinate in equation (9) and is given by

$$z(r) = 1 - 2\,\mathrm{e}^{-c_1 r}, \tag{13}$$

which maps the $r \in [0, \infty]$ interval to the $z \in [-1, 1]$ reduced interval, and finally $\chi(r;\, c_2,..., c_6)$ is an r-dependent term parametrically dependent on 5 c_k parameters to be fitted and is given by

$$\chi(r; c_2, ..., c_6) \frac{(1 - \mathrm{e}^{-c_2 r})^3}{\sqrt{(r^2 - c_3^2)^2 + c_4^2}\sqrt{(r^2 - c_5^2)^2 + c_6^2}}.$$

Our fitted $X\,^3\Sigma^-$ DMC is illustrated with its residual to the *ab initio* DMC in Fig. 4.

The irregular DMC has the desirable properties of quickly converging to the correct long-range limit, having enough parameters (13) to ensure an accurate description of the full range in bond length with minimal local oscillations, and provide a straight Normal Intensity Distribution Law (NIDL) (Medvedev 2012; Medvedev et al. 2015; Medvedev & Ushakov 2022)

5 LINE LIST

We produce a semi-empirical rovibronic line list SOLIS for $^{32}S^{16}O$ covering the $X\,^3\Sigma^-$, $a\,^1\Delta$, $b\,^1\Sigma^+$, and $A\,^3\Pi$ electronic states, where a system involving couplings between $X\,^3\Sigma^-$, $a\,^1\Delta$, $b\,^1\Sigma^+$, $A\,^3\Pi$, $B\,^3\Sigma^-$, $A''\,^3\Sigma^+$, $A'\,^3\Delta$, and $e\,^1\Pi$ defines our spectroscopic model. The SOLIS line list covers wavelengths down to 222.22 nm. Illustrations of the spectra simulated with the new line list are presented in Figures 5. and 6.

For nuclear motion calculations, a vibrational sinc-DVR basis set was defined for a grid of 301 internuclear geometries in the range 0.6–6.0 Å. We select 58 vibrational wavefunctions for the $X\,^3\Sigma^-$, $a\,^1\Delta$, $b\,^1\Sigma^+$, $A\,^3\Pi$, $B\,^3\Sigma^-$, $A''\,^3\Sigma^+$, $A'\,^3\Delta$, and $e\,^1\Pi$ states to form the contracted vibronic basis. In total, 7008 190 Einstein A coefficients between 84 114 bound rovibronic states were computed with a maximum total rotational quantum number $J_{\rm max} = 250$.

The PEC of the $A\,^3\Pi$ state implies that predissociative and continuum states should exist for the region above dissociation. To this end, these states have been removed from the line list through checking the character of the wavefunctions at the 'right' simulation border $r_{\rm max}$ in our DUO model where unbound states tend to oscillate at $r \to \infty$ with a non-zero density around $r_{\rm max}$ (Yurchenko et al. 2022). The line list we present therefore only contains bound-to-bound transitions only.

The calculated energies in the `.states` file are 'MARVELized' which involves replacing them with the MARVEL ones. For levels that are not covered by the MARVEL SN, the predicted shift method of Bowesman et al. (2021) was used to MARVELize them. Predicted shifts work by fitting the Obs. – Calc. trends as functions of J for each 'state', v and Ω energy band to then interpolate gaps within the MARVEL network or extrapolating to higher J.

The SOLIS line list is available in the ExoMol database (https://www.exomol.com/) in the form of a States (`.states`) and Transition (`.trans`) files, with extracts shown in Tables 3 and 4, respectively uncertainties for the energy levels where either taken directly as the MARVEL ones where available, or otherwise computed using the following empirical formulae

$$\sigma(\text{state}, J, v) = \Delta T + \Delta\omega\, v + \Delta B\, J(J+1), \tag{14}$$

where σ is the energy uncertainty for a given state and ΔT, $\Delta\omega$, ΔB are state dependent parameters given in Table 5. ΔT were found by taking twice the standard deviation of the total Obs. – Calc. of each electronic state (see Fig. 3) after outliers where removed by selecting states outside of this two standard deviation threshold, where the standard deviation was computed again.

5.1 Intensity scaling: dipoles and lifetimes

There are only a few recorded experimental values for electric dipole moments, lifetimes, and no direct intensity measurements which can be used to constrain our *ab initio* dipoles. Lifetimes are useful to constrain dipole moments via the relation

$$\frac{1}{\tau_u} = \sum_l A_{ul} \propto |\langle u|\mu_\sigma|\tilde{l}\rangle|^2, \tag{15}$$

where $|\tilde{l}\rangle$ is the dominant ro-vibronic state contributing to the lifetime of the level $|u\rangle$, $\sigma = 0, \pm 1$ denotes a tensorial dipole component. So a scaling in lifetime $\tilde{\tau} = \xi\tau$ would correspond to an approximate scaling in dipole moment to the dominant lower state of $1/\sqrt{\xi}$.

Previous Stark measurements (Powell & Lide 1964; Lovas et al. 1992) have determined the ground state dipole to be $\mu_X^0 =$ 1.55(2) D (Powell & Lide 1964) and 1.52(2) D (Lovas et al.

Table 3. Extract from the states file of the line list for SO.

i	Energy (cm^{-1})	g_i	J	unc	τ	Parity		State	v	Λ	Σ	Ω	Ma/Ca	Energy (cm^{-1})
733	12 277.658 473	5	2	0.302 298	0.068 323	+	e	a1Delta	6	2	0	2	Ca	12 277.658 473
734	12 576.557 170	5	2	0.010 390	0.006 7518	+	e	b1Sig+	2	0	0	0	Ma	12 576.558 535
735	12 824.746 272	5	2	0.603 962	0.025 301	+	e	X3Sig–	12	0	0	0	Ca	12 824.746 272
736	12 836.684 546	5	2	0.603 962	0.025 272	+	e	X3Sig–	12	0	1	1	Ca	12 836.684 546
737	13 297.933 546	5	2	0.352 298	0.059 146	+	e	a1Delta	7	2	0	2	Ca	13 297.933 546
738	13 602.425 655	5	2	0.165 193	0.006 9414	+	e	b1Sig+	3	0	0	0	PS	13 601.834 707
739	13 810.582 705	5	2	0.653 962	0.023 019	+	e	X3Sig–	13	0	0	0	Ca	13 810.582 705
740	13 822.577 830	5	2	0.653 962	0.022 993	+	e	X3Sig–	13	0	1	1	Ca	13 822.577 830

Notes. i is the state counting number. $\tilde{E}$ is the state energy term values in cm^{-1}, MARVEL or Calculated (Duo). g_i is the total statistical weight, equal to $g_{ns}(2J + 1)$. J is the total angular momentum. unc is the uncertainty, cm^{-1}. τ is the lifetime (s^{-1}). +/− is the total parity. *e/f* is the rotationless parity. State is the electronic state. v is the State vibrational quantum number. Λ is the projection of the electronic angular momentum. Σ is the projection of the electronic spin. Ω is the projection of the total angular momentum, $\Omega = \Lambda + \Sigma$. Label refers to the data source, 'MA' is for MARVEL 'Ca' is for Calculated, and 'PS' is for predicted shift. Energy is the State energy term values in cm^{-1}, calculated (Duo).

Table 4. Extract from the transitions file of the line list for SO.

f	i	A_{fi} (s^{-1})	$\tilde{\nu}_{fi}$
37 557	36 527	2.7817E-01	5199.704 942
37 204	36 852	2.7817E-01	5199.704 945
32 098	32 422	1.2080E+00	5199.713 048
21 055	22 048	3.3851E-06	5199.718 029
60 350	61 047	2.8777E-04	5199.728 151
45 755	46 561	4.3835E-01	5199.728 902

Notes. f is the upper state counting number. i is the lower state counting number. A_{fi} is the Einstein-A coefficient in s^{-1}. $\tilde{\nu}_{fi}$ is the transition wavenumber in cm^{-1}.

Table 5. State-dependent parameters (in cm^{-1}) of equation (14) used to estimated uncertainties for the calculated states of $^{32}S^{16}O$ where MARVEL uncertainties were not available.

State	ΔT	$\Delta\omega$	ΔB
$X\,^3\Sigma^-$	0.003 363	0.05	0.0001
$a\,^1\Delta$	0.001 698	0.05	0.0001
$b\,^1\Sigma^+$	0.368 965	0.05	0.0001
$A\,^3\Pi$	2.835 039	0.05	0.0001

1992), slightly smaller than our computed vibrational transition moment of $|\langle X\,^3\Sigma^-, v = 0|\mu_0|X\,^3\Sigma^-, v = 0\rangle| = 1.588$ D. We scale our $X\,^3\Sigma^-$ dipole to the value of 1.535 D averaged from the two Stark measurements, which we note is the dipole moment adopted by CDMS (Endres et al. 2016) where the same averaging was done. Wildt et al. (1983) measure the radiative lifetime of the $b\,^1\Sigma^+(v = 0)$ state through time-resolved measurements of the $b\,^1\Sigma^+ \rightarrow X\,^3\Sigma^-$ emission band and provide a lifetime of $\tau = 6.8 \pm 0.4$ ms. To achieve this lifetime, we scale our $\langle b\,^1\Sigma^+|\mu_0|b\,^1\Sigma^+\rangle$ dipole by a factor of 0.7401.

Saito (1970) determines the $a\,^1\Delta$ dipole moment to be 1.336 ± 0.045 D through Stark measurements, larger than our computed transition moment $|\langle a\,^1\Delta, v = 0|\mu_0|a\,^1\Delta, v = 0\rangle| = 1.184$ D. We scale our $a\,^1\Delta$ dipole by a factor of 1.1282 to reproduce the measured transition moment.

Radiative lifetimes of the $A\,^3\Pi$ state for $v' = 0 - 13$ were measured by Elks & Western (1999) by laser-induced fluorescence and Clyne & Liddy (1982) for $v' = 0 - 6$. Fig. 7 shows the experimentally determined lifetimes as a function of v' with the theoretically predicted values by Borin & Ornellas (2000) and Fulscher et al. (1992) and those computed by our model superimposed in red. Since Elks & Western (1999) quote their lifetimes to a lower uncertainty and for a large vibrational coverage, we chose to model their lifetimes. Modelling these lifetimes proved to be difficult, the characteristic sharp drop in lifetime from $v' = 0$ and 1 was very sensitive to multiple factors: (1) the position of the $\langle A\,^3\Pi|\mu_{\pm1}|X\,^3\Sigma^-\rangle$ dipole relative to the respective PECs; (2) the crossing point of the dipole with zero; (3) the local gradient of the dipole around the zero crossing point. Initial attempts to reproduce the experimental lifetimes were made using our *ab initio* dipole, various *ab initio* dipoles from the literature (Fulscher et al. 1992; Feng & Zhu 2019; Sarka & Nanbu 2019), and the empirical dipole from Elks & Western (1999) in our model all failed to produce lifetimes that agreed with experiment.

Firstly, we were able to reproduce the lifetimes of Elks & Western (1999) using a linear dipole function. Albeit being non-physical, it provided important constraints on the short-range position and its gradient around the equilibrium geometry. We then combined it with the MRCI-F12+Q/aug-cc-pV(5 + d)Z dipole computed by Sarka & Nanbu (2019) at larger values of r into a single smooth curve. Despite a slight change in the shape of the *ab initio* dipole, Fig. 7 shows that our semi-empirically fitted $\langle A\,^3\Pi|\mu_{\pm1}|X\,^3\Sigma^-\rangle$ dipole is much closer to the *ab initio* curve than the empirically fitted dipole by Elks & Western (1999).

5.2 Partition function

We compute the molecular partition function (PF) for SO from our semi-empirical line list using

$$Q(T) = \sum_i g_i^{\rm tot} e^{-\frac{c_2 \tilde{E}_i}{T}} \tag{16}$$

where c_2 is the second radiation constant, $\tilde{E}_i$ is the rovibronic energy term value in wavenumbers, $g_i^{\rm tot} = g_{ns}(2J_i + 1)$ is the total state degeneracy which includes the nuclear weight spin-statistic g_{ns} ($g_{ns} = 1$ for $^{32}S^{16}O$) where we use a 1 K temperature step. Fig. 8 compares our computed PF to the PFs of Sauval & Tatum (1984), Barklem & Collet (2016), CDMS (Endres et al. 2016), and Hitran (Gamache et al. 2017) who compute their PF from the line lists produced by Bernath, Johnson & Liévin (2021), Bernath, Johnson & Liévin (2022). As the nuclear spin degeneracy is one, no PFs need to be scaled to the physics convention of nuclear statistical weights, which ExoMol uses. Fig. 8 shows that all PFs agree for $500 \lesssim T \lesssim 2000$ K; for all temperatures, our computed PF continues to agree with that of Barklem & Collet (2016), where our computed PF is generally lower than theirs up to 0.1 per cent at 5000 K; the CDMS PF agrees to within 1 per cent of all PFs up to it cutoff at 300 K; Sauval & Tatum

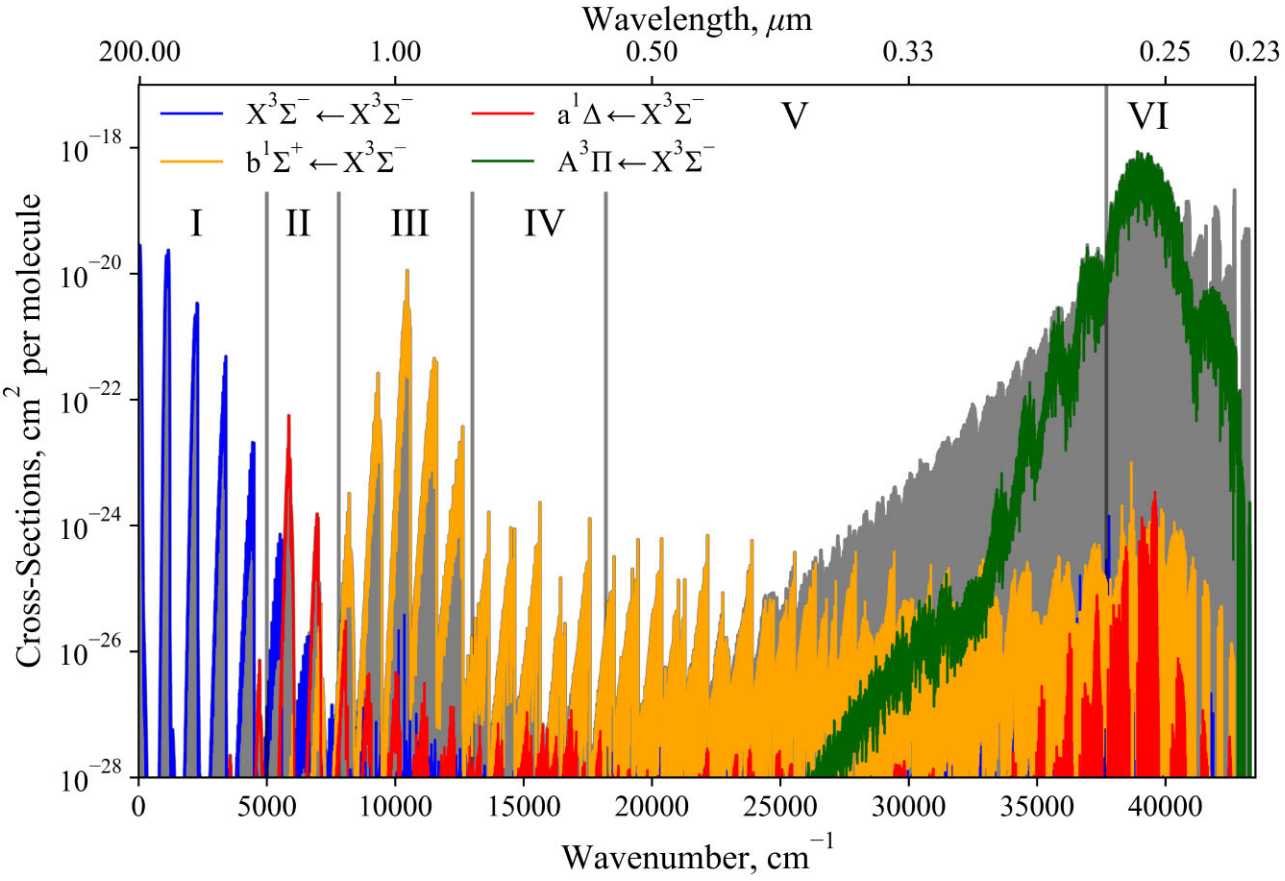

Figure 5. Dipole allowed and forbidden components of the absorption spectrum simulated with our semi-empirical model at 1000 K connecting $X\,^3\Sigma^-$ with $X\,^3\Sigma^-$, $a\,^1\Delta$, $b\,^1\Sigma^+$, and $A\,^3\Pi$. Regions of spectral importance are marked with roman numerals and are detailed in the text. The grey-shaded region marks the total SO opacity computed with our model at 1000 K.

(1984) is larger than the rest of the PFs at low temperatures up to 500 and at 5000 K their PF is 3.4 per cent lower than our computed PF; the HITRAN PF begins to deviate from the other PFs from about 2000 K, where at 5000 K it is lower than ours by 17 per cent; this behaviour of HITRAN PFs has been noted previously (Wang et al. 2023).

5.3 SO opacities

We follow the ExoMolOP procedure of Chubb et al. (2020) and generate molecular opacitites for SO using the SOLIS line list for four exoplanetary atmosphere retrieval codes ARCiS (Min et al. 2020), TauREx (Al-Refaie et al. 2021), NEMESIS (Irwin et al. 2008), and petitRADTRANS (Molliére et al. 2019) on an extensive grid of temperatures and pressures. The opacities are provided as part of the SO ExoMol data set at www.exomol.com.

5.4 Simulated spectra

Program EXOCROSS (Yurchenko, Al-Refaie & Tennyson 2018b) was used to simulate rovibronic absorption spectra as a function of temperature using SOLIS. Fig. 5 illustrates the dipole allowed and forbidden electronic bands connecting the $X\,^3\Sigma^-$ state to $X\,^3\Sigma^-$, $a\,^1\Delta$, $b\,^1\Sigma^+$, and $A\,^3\Pi$ which are shown as different colours and the total computed SO opacity is shown in grey. Here, we simulate lines with a Gaussian line profile of HWHM 0.6 cm^{-1}. The forbidden band intensities are stolen through mixing of the electronic wavefunctions through couplings such as SOCs, DMCs, and EAMCs resulting in non-zero dipole matrix elements, which we note provides a stronger mechanism here than their corresponding magnetic dipole or electric quadrupole couplings. Fig. 6 shows the temperature variation of the simulated total SO opacity which has a strong effect on the UV/Vis cross-sections. The greatest temperature variation can be seen in the 18 000–35 000 cm^{-1} region (V) where the $X\,^3\Sigma^- \rightarrow B\,^3\Sigma^-$ band begins to dominate opacity. Here we simulate lines with a Gaussian line profile of HWHM 0.6 cm^{-1}. It is clear the IR/NIR spectrum is largely unaffected by the increase of temperature except from the expected rotational broadening. Below, we comment on the spectral regions marked by I–VI illustrated in Fig. 5.

(I) The IR ∼0–5000 cm^{-1} region is dominated by the $X\,^3\Sigma^- \leftarrow X\,^3\Sigma^-$ electronic band peaking at $\sim 3 \times 10^{-20}$ cm^2 per molecule.

(II) The ∼5000–7800 cm^{-1} NIR region shows strong $a\,^1\Delta \leftarrow X\,^3\Sigma^-$ band features, even for room temperature spectra, but $X\,^3\Sigma^- \leftarrow X\,^3\Sigma^-$ lines are expected to be still observable here.

(III) The ∼7800–13000 cm^{-1} NIR region is dominated by strong $b\,^1\Sigma^+ \leftarrow X\,^3\Sigma^-$ band absorption for all temperatures, and is almost as strong as the dipole allowed $X\,^3\Sigma^- \leftarrow X\,^3\Sigma^-$ band spectrum because of large intensity stealing mechanism facilitated through the strong $\langle b\,^1\Sigma^+|\mu_z|X\,^3\Sigma^-\rangle$ SOC, see the Appendix.

(IV) The Vis ∼13000–18200 cm^{-1} region shows a flat feature due to $A\,^3\Pi \leftarrow X\,^3\Sigma^-$ band absorption which becomes prominent for temperatures above 3000 K. However, since we omit the $C\,^3\Pi$

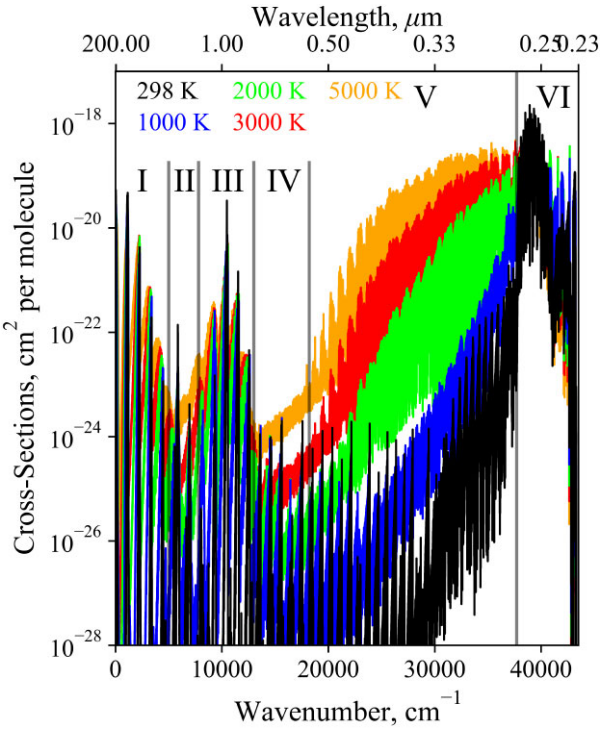

Figure 6. The total absorption spectrum of SO simulated with our semi-empirical model for different temperatures ranging from 298 to 5000 K. We see the intensity deviation is greatest in region *V* around 18 000–35 000 cm^{-1} where the $B\,^3\Sigma^- \leftarrow X\,^3\Sigma^-$ band begins to dominate opacity.

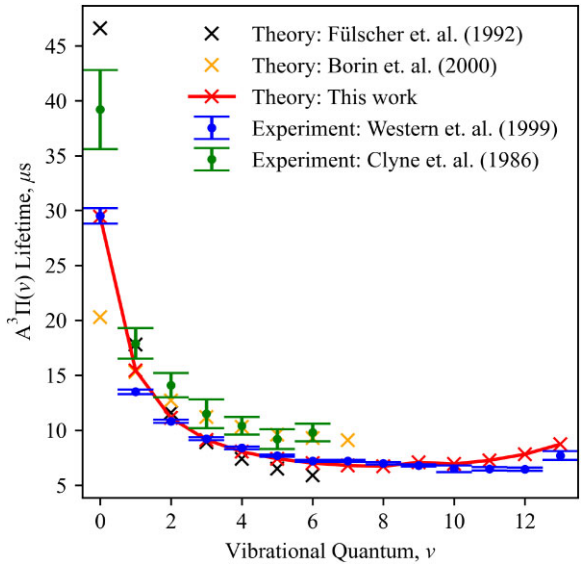

Figure 7. The $A\,^3\Pi$ lifetimes as a function of v' are shown from experimental (Clyne & Tennyson 1986; Elks & Western 1999) and theoretical (Fulscher et al. 1992; Borin & Ornellas 2000) sources with our computed lifetimes overlaid in red.

state in our spectroscopic model we do not compute $C\,^3\Pi \leftarrow A'\,^3\Delta$ and $C\,^3\Pi \leftarrow A''\,^3\Sigma^+$ band intensities which we previously predicted to be strong in this region (Brady et al. 2022).

(V) The Vis/UV ∼18200–37700 cm^{-1} region is largely uncovered at high accuracy by our spectroscopic model since it is dominated by the $B\,^3\Sigma^- \leftarrow X\,^3\Sigma^-$ and lesser $C\,^3\Pi \leftarrow X\,^3\Sigma^-$ electronic bands

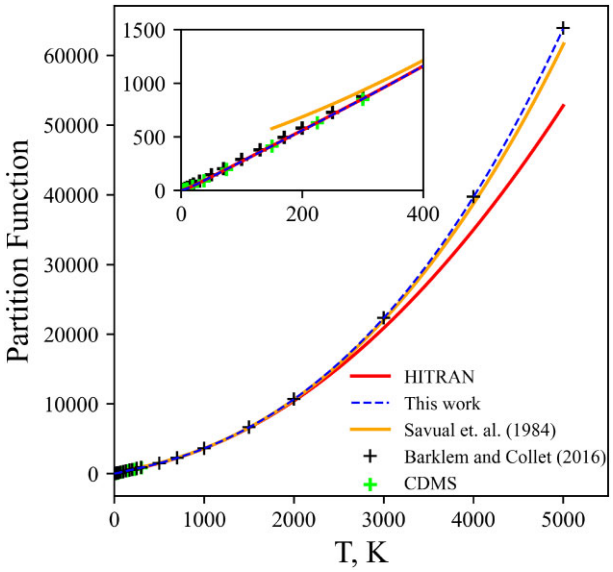

Figure 8. Comparison between our PF and those produced by HITRAN (Gamache et al. 2017), Sauval & Tatum (1984), Barklem & Collet (2016), and CDMS (Endres et al. 2016).

which become major sources of SO opacity for temperatures above 1000 K. We are currently working on the UV SO line list for a future study which will accurately cover this region. However, for lower temperatures, the $A\,^3\Pi \leftarrow X\,^3\Sigma^-$ and $b\,^1\Sigma^+ \leftarrow X\,^3\Sigma^-$ bands become more important which we recover accurately in this study.

(VI) The UV ∼37700–43500 cm^{-1} region has a strong $A\,^3\Pi \leftarrow X\,^3\Sigma^-$ band feature which should be observable at all temperatures.

5.5 Comparisons to experimental spectra

There are few recorded experimental spectra of $^{32}S^{16}O$ with large coverage and almost none with absolute intensity measurements, relative intensities are usually provided (Burkholder et al. 1987; Setzer, Fink & Ramsay 1999; Chu et al. 2002; Wang et al. 2005). The only study to our knowledge that provides measured absolute intensities is the recent study by Heays et al. (2022) on the $A\,^3\Pi - X\,^3\Sigma^-$ band, which we compare to (also $B\,^3\Sigma^- - X\,^3\Sigma^-$ and $C\,^3\Pi - X\,^3\Sigma^-$ bands which we do not compare to).

The forbidden band intensities we compute here are through the intensity stealing mechanism which works through mixing of electronic state wavefunctions through couplings such as SOCs. We do not compute magnetic dipole intensities, which are much weaker for the bands of interest than the redistributed intensities which we compute. For example, the diagonal $\langle b\,^1\Sigma^+|\mu_z|b\,^1\Sigma^+\rangle$ and $\langle X\,^3\Sigma^-|\mu_z|X\,^3\Sigma^-\rangle$ dipoles produce $b\,^1\Sigma^+ \leftarrow X\,^3\Sigma^-$ band intensities a factor of ∼10−1000 times stronger at the band peak than the corresponding magnetic dipole intensities. Therefore, we omit magnetic dipole transitions from our line list. An example of the intensity stealing mechanism is given in Appendix.

5.5.1 *Hitran*

HITRAN produces empirical SO line lists which have been produced by fitting spectroscopic models to experimentally derived spectroscopic constants, lifetimes, and rotational branching ratios (ratios in perpendicular and parallel transition moments, see below

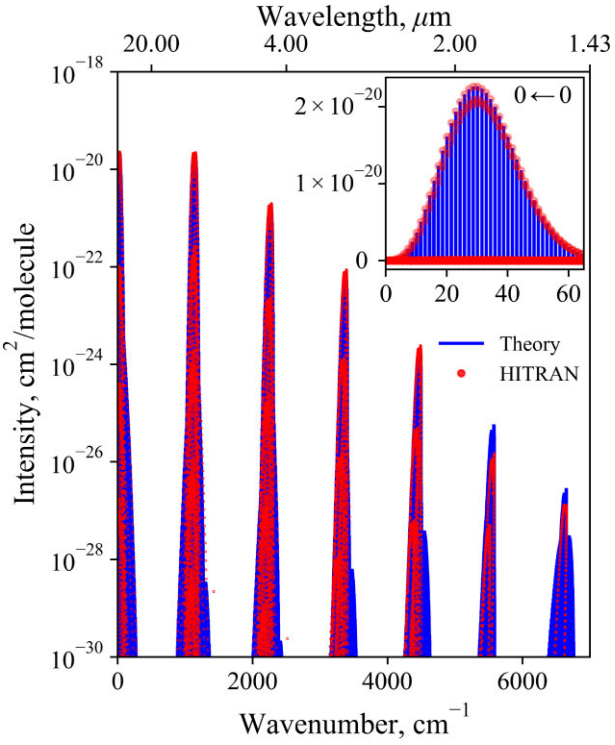

Figure 9. Comparison between the theoretical and HITRAN $X\,^3\Sigma^- \rightarrow X\,^3\Sigma^-$ rovibrational band for 0–7000 cm^{-1}. We simulate the spectra using a temperature of 296 K and scale the intensities by the fractional isotopologue abundance of 0.9479 (Gordon et al. 2022).

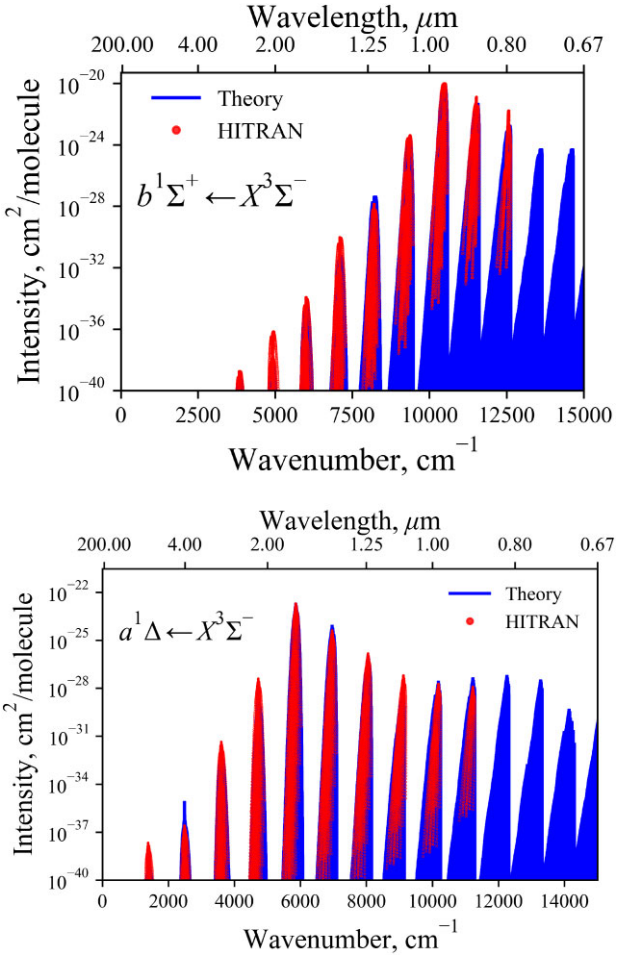

Figure 10. Comparison between the theoretical and HITRAN $b\,^1\Sigma^+ \rightarrow X\,^3\Sigma^-$ (top panel) and $a\,^1\Delta \rightarrow X\,^3\Sigma^-$ (bottom panel) absorption spectrum for 0–15000 cm^{-1}. We simulate the spectra using a temperature of 296 K and scale the intensities by the fractional isotopologue abundance of 0.9479 (Gordon et al. 2022).

discussion), hence we will compare to this data since it is the closest comparison of rovibronic intensities to experimental data for the $X\,^3\Sigma^- - X\,^3\Sigma^-$, $b\,^1\Sigma^+ - X\,^3\Sigma^-$, and $a\,^1\Delta - X\,^3\Sigma^-$ electronic bands.

HITRAN (Gordon et al. 2022) provides empirical line list data on the first three electronic states of SO $X\,^3\Sigma^-$, $a\,^1\Delta$, and $b\,^1\Sigma^+$ to which we compare our theoretical spectra to. The HITRAN intensities for the $X\,^3\Sigma^- \leftarrow X\,^3\Sigma^-$ band were originally presented by Bernath, Johnson & Liévin (2022) and the forbidden $b\,^1\Sigma^+ \leftarrow X\,^3\Sigma^-$ and $a\,^1\Delta \leftarrow X\,^3\Sigma^-$ bands are from Bernath, Johnson & Liévin (2021). In both studies, fitted spectroscopic constants from the literature were used to predict line positions, transition moments were obtained using LeRoy's LEVEL program (Le Roy 2017) which assumes the single state approximation, and their line lists were computed using PGOPHER (Western 2017). Bernath, Johnson & Liévin (2021) used Ω-representation to allow for the single state approximation in line with LEVEL such that the forbidden band intensity are computed from effective dipoles between single Ω-states, the so-called parallel and perpendicular transition moments, as opposed to the non-approximate intensity stealing mechanism via mixing of electronic wavefunctions through, for example, SOCs, as we do. Perpendicular and parallel electronic transition moments between the spin-orbit states $b0^+ - X0^+$, $b0^+ - X1$, and $a2 - X1$ (see appendix) were computed by Bernath, Johnson & Liévin (2021) at an iC-MRCI/aug-cc-pCVQZ-DK level of theory and were scaled to the experimentally determined values by Setzer, Fink & Ramsay (1999). The HITRAN $X\,^3\Sigma^- \leftarrow X\,^3\Sigma^-$ intensities were computed using the *ab initio* ground state expectation dipole moment computed by Bernath, Johnson & Liévin (2022) at a ic-MRCI+Q/ACV6Z-X2C/ED + Q level of theory.

In all comparisons below, we scale our computed intensities with the $^{32}S^{16}O$ isotopologue abundance 0.947926 given by HITRAN (Gordon et al. 2022). Fig. 9 presents a comparison between our semi-empirical $X\,^3\Sigma^- \leftarrow X\,^3\Sigma^-$ rovibronic spectrum, where we compute stick spectrum using a temperature of 296 K, and the empirical HITRAN line list (Bernath, Johnson & Liévin 2022). We see good agreement in both the line positions and band structure where band intensities agree up to the fifth hot band at ∼ 4500 cm^{-1} where we compute higher intensities relative to the HITRAN data. The $0 \leftarrow 0$ band agrees extremely well which can be seen in the sub plot of Fig. 9. The agreement in intensities confirms our methodology since the HITRAN dipole was also scaled to the same experimental values discussed in Section 5.1. The discrepancy in intensities towards hotter bands can be attributed to the difference in the DMCs as well as the wavefunctions used to calculate the transition probabilities.

Fig. 10 compares our computed $b\,^1\Sigma^+ \leftarrow X\,^3\Sigma^-$ spectrum simulated at a temperature of 296 K to the empirical HITRAN (Gordon et al. 2022) $b\,^1\Sigma^+ \leftarrow X\,^3\Sigma^-$ line list (Bernath, Johnson & Liévin 2021). For this comparison, we filtered out the magnetic dipole transitions present in the HITRAN line list, since we only calculate electric dipole transitions. The selection rules for magnetic dipole branches are the same except they follow the non-parity changing rule. We see that our model supplements the HITRAN line list at both the higher and lower wavenumber regions (< 4000 and >

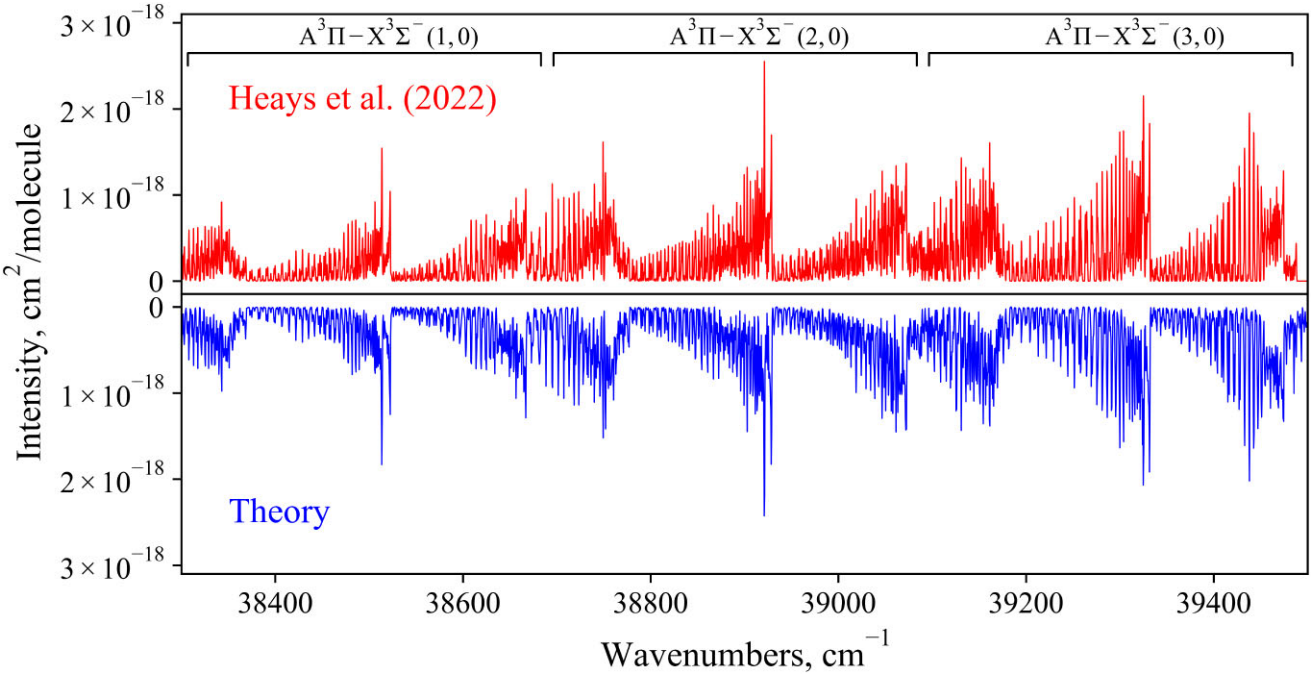

Figure 11. Comparison of our computed absorption $A\,^3\Pi(v' = 1, 2, 3) - X\,^3\Sigma^-(v'' = 0)$ band to the cross-sections generated from Heays et al. (2022) empirical line list fitted band-by-band to their measured spectra.

12500 cm^{-1}) where line positions, band structure and intensities generally show good agreement which is to be expected since the HITRAN $b\,^1\Sigma^+ \leftarrow X\,^3\Sigma^-$ dipoles were scaled to the same experimental values for the $b\,^1\Sigma^+$ lifetime as we do. For vibrational bands energetically below $\sim$ 7500 cm^{-1}, the two spectra begin to deviate from each other, where SOLIS tends to be slightly lower than the HITRAN intensities. However, this is below the standard HITRAN intensity threshold of 10^{-30} cm^2/molecule, and so these bands are typically of less importance. For intensities above the threshold, we see good agreement in line with the methodologies used.

We also compare to the forbidden $a\,^1\Delta \leftarrow X\,^3\Sigma^-$ band in Fig. 10 to the theoretical HITRAN line list at 296 K. The transitions here are all electric dipole in nature. We see the electronic band structure agrees well between the peak band up to the penultimate hot band before the HITRAN terminus at $\sim$11000 cm^{-1} with the largest intensity deviation being between vibronic bands outside the 5000–8500 cm^{-1} spectral range. The low-energy bands <4500 cm^{-1} all sit below the 10^{-30} cm^2/molecule intensity threshold, which are less important spectroscopically. Differences in the band intensity are difficult to disentangle since $a\,^1\Delta \leftarrow X\,^3\Sigma^-$ is a dipole forbidden band where intensities are accumulated through 'intensity stealing' mechanism via multiple coupling channels in our model.

The general agreement with the empirical HITRAN line list confirms we are not missing any fundamental physics since we both produce similar spectra using a different methodology. Furthermore, Bernath, Johnson & Liévin (2021) scale their $b\,^1\Sigma^+ \leftarrow X\,^3\Sigma^-$ effective dipoles using the same lifetime provided by Setzer, Fink & Ramsay (1999) as we did, whereas the $a\,^1\Delta \leftarrow X\,^3\Sigma^-$ band have no reliable experimental dipoles or lifetimes to scale the *ab initio* dipoles to except the indirect $a\,^1\Delta - a\,^1\Delta$ dipole moment presented by (Saito 1970) which only we scale to. Agreement for the latter band then confirm the good quality of the PECs, SOCs, and (T)DMCs used.

5.5.2 *A–X bands*

The recent study by Heays et al. (2022) measured, in high resolution, the FUV $A\,^3\Pi - X\,^3\Sigma^-$ band via Fourier-transform spectroscopy up to the $(v', v'') = (3, 0)$ band for $J \leq 51$; the $B\,^3\Sigma^- - X\,^3\Sigma^-$ and $C\,^3\Pi - X\,^3\Sigma^-$ bands were also measured but we do not compare to these here. Heays *et al.* present an empirical line list where effective Hamiltonian spectroscopic constants were fitted band-by-band to their measured spectrum, providing quantum number assignments and oscillator strengths for each assigned transition. Their coupled-band models reproduce the experimentally measured line positions, intensities, and widths to within 5 per cent uncertainty. With this, we converted their line list to the EXOCROSS format to compute corresponding cross-sections, which we compare to. For all spectra simulations a temperature of T = 360 K and Gaussian line broadening of HWHM 0.3 cm^{-1} was used. Fig. 11 shows the comparison between our computed $A\,^3\Pi(v' = 1, 2, 3) - X\,^3\Sigma^-(v'' = 0)$ band intensities in blue (bottom panel) and the simulated band intensities of Heays et al. (2022) in red (top panel). We see excellent agreement in line positions, intensities, and band structure, where a mirror plot was chosen since overlaying the spectra made it hard to distinguish between them since they agree so well.

We are confident that our model correctly reproduces the experimental spectra for the $A\,^3\Pi(v' = 1, 2, 3) - X\,^3\Sigma^-(v'' = 0)$ band, confirming the good quality of our PECs, (T)DMCs, and couplings to other states.

6 CONCLUSION

We present the semi-empirical SOLIS line list for $^{32}S^{16}O$ constructed starting from the refinement of the *ab initio* spectroscopic model presented by Brady et al. (2022) to empirically derived energy levels, or MARVEL energy levels. As part of the line list creation, a MARVEL analysis of 29 experimental transition sources resulted in a self-consistent set of 8558 rotation–vibration energy levels (J

≤ 69 and $v \leq 3$) for the $X\,^3\Sigma^-$, $a\,^1\Delta$, $b\,^1\Sigma^+$, $A\,^3\Pi$, $B\,^3\Sigma^-$, $C\,^3\Pi$ electronic states, where 48 972/50 106 experimental transitions were validated. The SOLIS SO line list supplements existing ExoMol line lists for SO_2 (Underwood et al. 2016a) and SO_3 (Underwood et al. 2016b).

The $X\,^3\Sigma^-$ state expectation value of the dipole moment operator was fitted to an analytical form and shown to improve the non-physical flattening of the vibrational transition moment and NIDL compared to using the grid interpolated form of the DMC. This resulted the physical exponential decay of the $X\,^3\Sigma^- \rightarrow X\,^3\Sigma^-$ IR spectral band.

Comparison of the simulated rovibronic spectrum of SO to experiment/HITRAN show good agreements in both positions and intensities. However, inspection of the $v = 0 \rightarrow 0$ of the forbidden $b\,^1\Sigma^+ \rightarrow X\,^3\Sigma^-$ band revealed disagreeing P- and R-branch ratios to experiment, where tuning of the spectroscopic model showed no proper inversion of the branch intensities. Analysis of the electronic wavefunctions revealed that the band intensities are dominated by competing diagonal *X* and *b* DMCs, which contribute to the parallel transition moment. The weaker perpendicular transition moment was shown to produce intensities of the desired P- and R-branch ratio, but was much weaker than the parallel transition component to the intensities. Analysis on the basis set revealed the branch ratio to be more sensitive when including a larger vibrational basis, but still does not produce the desired branch ratio.

The future work includes extension to the UV region with the $B\,^3\Sigma^- \leftarrow X\,^3\Sigma^-$ and $C\,^3\Pi \leftarrow X\,^3\Sigma^-$ electronic bands, and production of photodissociation cross-sections and rates.

ACKNOWLEDGEMENTS

This work was supported by the European Research Council (ERC) under the European Union's Horizon 2020 research and innovation programme through advance grant number 883830 and the STFC Projects No. ST/M001334/1 and ST/R000476/.

DATA AVAILABILITY

The states, transition, opacity, and PF files for the SO line lists are provided via www.exomol.com. The open-access programs DUO and EXOCROSS are available from github.com/exomol.

REFERENCES

Al-Refaie A. F., Changeat Q., Waldmann I. P., Tinetti G., 2021, ApJ, 917, 37
Amin M. Y., Elnawawy M. S., Elshalaby M. A., 1991, Astrophys. Space Sci., 185, 277
Bachiller R., 1996, ARA&A, 34, 111
Barklem P. S., Collet R., 2016, A&A, 588, A96
Belyaev D. A. et al., 2012, Icarus, 217, 740
Bernath P. F., Johnson R., Liévin J., 2021, J. Quant. Spectrosc. Radiat. Transf., 272, 107772
Bernath P. F., Johnson R., Liévin J., 2022, J. Quant. Spectrosc. Radiat. Transf., 290 108317
Bielefeld M., Elfers G., Fink E. H., Kruse H., Wildt J., Winter R., Zabel F., 1984, J. Photochem., 25, 419
Blake G. A., Sutton E. C., Masson C. R., Phillips T. G., 1987, AJ., 315, 621
Bogey M., Demuynck C., Destombes J. L., 1982, Chem. Phys., 66, 99
Bogey M., Civis S., Delcroix B., Demuynck C., Krupnov A. F., Quiguer J., Tretyakov M. Y., Walters A., 1997, J. Mol. Spectrosc., 182, 85
Borin A. C., Ornellas F. R., 2000, Chem. Phys. Lett., 322, 149
Bouchoux A., Marchand J., Janin J., 1971a, Spectrochim. Acta, 27, 1909
Bouchoux A. M., Marchand J., Janin J., 1971b, Spectra Chimica Acta A, A27, 1909
Bouchoux A. M., Marchand J., Janin J., 1972, Cr. Acad. Sci. B Phys., 274, 256
Bouchoux M. A.-M., Marchand M., 1972, Spectra Chimica Acta A, 28, 1771
Bowesman C. A., Shuai M., Yurchenko S. N., Tennyson J., 2021, MNRAS, 508, 3181
Brady R. P., Yurchenko S. N., Kim G.-S., Somogyi W., Tennyson J., 2022, Phys. Chem. Chem. Phys. 24 24076–24088
Brown J. M., Merer A. J., 1979, J. Mol. Spectrosc., 74, 488
Burkholder J. B., Lovejoy E. R., Hammer P. D., Howard C. J., Mizushima M., 1987, J. Mol. Spectrosc., 124, 379
Cazzoli G., Lattanzi V., Coriani S., Gauss J., Codella C., Ramos A. A., Cernicharo J., Puzzarini C., 2017, A&A, 605, A20
Cazzoli G., Cludi L., Cotti G., Esposti C. D., Dore L., 1994, J. Mol. Spectrosc., 167, 468
Chernin L., Masson C., 1993, ApJ, 403, L21
Chu Y. N., Wang H. M., Li J. Q., Cheng P., Cao D. Z., 2002, Chem. Phys. Lett., 366, 147
Chubb K. L. et al., 2020, A&A, 646, A21
Clark W. W., Delucia F. C., 1976, J. Mol. Spectrosc., 60, 332
Clark F. O., Johnson D. R., 1974, ApJ, 191, L87
Clyne M. A. A., Liddy J. P., 1982, J. Chem. Soc. Faraday Trans., 78, 1127
Clyne M. A. A., Tennyson P. H., 1986, J. Chem. Soc. Faraday Trans., 82, 1315
Codella C., Muders D., 1997, MNRAS, 291, 337
Colin R., 1968, Can. J. Phys., 46, 1539
Colin R., 1969, Can. J. Phys., 47, 979
Colin R., 1982, J. Chem. Soc. Faraday Trans., 78, 1139
Császár A. G., Furtenbacher T., 2011, J. Mol. Spectrosc., 266, 99
de Pater I., Roe H., Graham J. R., Strobel D. F., Bernath P., 2002, Icarus, 156, 296
Elks J. M. F., Western C. M., 1999, J. Chem. Phys., 110, 7699
Endo Y., Kanamori H., Hirota E., 1987, Chem. Phys. Lett., 141, 129
Endres C. P., Schlemmer S., Schilke P., Stutzki J., Müller H. S. P., 2016, J. Mol. Spectrosc., 327, 95
Feng Y., Zhu Z., 2019, J. Quant. Spectrosc. Radiat. Transf., 234, 98
Fulscher M. P., Jaszunski M., Roos B. O., Kraemer W. P., 1992, J. Chem. Phys., 96, 504
Furtenbacher T., Császár A. G., 2012a, J. Quant. Spectrosc. Radiat. Transf., 113, 929
Furtenbacher T., Császár A. G., 2012b, J. Mol. Struct., 1009, 123
Furtenbacher T., Császár A. G., Tennyson J., 2007, J. Mol. Spectrosc., 245, 115
Gamache R. R. et al., 2017, J. Quant. Spectrosc. Radiat. Transf., 203, 70
Gaydon A. G., 1948, Spectroscopy and Combustion Theory, 2nd edn. Chapman and Hall, Ltd., London
Gordon I. E. et al., 2022, J. Quant. Spectrosc. Radiat. Transf., 277, 107949
Gottlieb C. A., Ball J. A., 1973, ApJ, 184, L59
Gottlieb C. A., Gottlieb E. W., Litvak M. M., Ball J. A., Penfield H., 1978, ApJ, 219, 77
Heays A. N., Stark G., Lyons J. R., de Oliveira N., Lewis B. R., Gibson S. T., 2022, Mol. Phys., 0, e2153092
Hobbs R., Rimmer P. B., Shorttle O., Madhusudhan N., 2021, MNRAS, 506, 3186
Huber K. P., Herzberg G., 1979, Molecular Spectra and Molecular Structure IV. Constants of Diatomic Molecules. Van Nostrand Reinhold Company, New York, NY
Irwin P. G. J. et al., 2008, J. Quant. Spectrosc. Radiat. Transf., 109, 1136
Kanamori H., Butler J. E., Kawaguchi K., Yamada C., Hirota E., 1985, J. Mol. Spectrosc., 113, 262
Kanamori H., Tiemann E., Hirota E., 1988, J. Chem. Phys., 89, 621
Kato H., 1993, Bull. Chem. Soc. Japan, 66, 3203
Kim E., Yamamoto S., 2003, J. Mol. Spectrosc., 219, 296
Klaus T., Belov S. P., Saleck A. H., Winnewisser G., Herbst E., 1994, J. Mol. Spectrosc., 168, 235
Klaus T., Saleck A. H., Belov S. P., Winnewisser G., Hirahara Y., Hayashi M., Kagi E., Kawaguchi K., 1996, J. Mol. Spectrosc., 180, 197

Klaus T., Belov S. P., Winnewisser G., 1997, J. Mol. Spectrosc., 186, 416
Kramida A., Ralchenko Y., Reader J., NIST ASD Team, 2020, Atoms, 8, 56
Krasnopolsky V. A., 2012, Icarus, 218, 230
Laas J. C., Caselli P., 2019, A&A, 624 A108
Le Roy R. J., 2017, J. Quant. Spectrosc. Radiat. Transf., 186, 167
Lee E. G., Seto J. Y., Hirao T., Bernath P. F., Le Roy R. J., 1999, J. Mol. Spectrosc., 194, 197
Lellouch E., 1996, Icarus, 124, 1
Lovas F. J., Suenram R. D., Ogata T., Yamamoto S., 1992, ApJ, 399, 325
Martin E. V., 1932, Phys. Rev., 41, 167
Martin-Drumel M. A., Hindle F., Mouret G., Cuisset A., Cernicharo J., 2015, AJ., 799, 115
Medvedev E. S., 2012, J. Chem. Phys., 137, 174307
Medvedev E. S., Ushakov V. G., 2022, J. Quant. Spectrosc. Radiat. Transf., 395 108255
Medvedev E. S., Meshkov V. V., Stolyarov A. V., Gordon I. E., 2015, J. Chem. Phys., 143, 154301
Medvedev E. S., Meshkov V. V., Stolyarov A. V., Ushakov V. G., Gordon I. E., 2016, J. Mol. Spectrosc., 330, 36
Miller H. C., Yamasaki K., Smedley J. E., Leone S. R., 1991, Chem. Phys. Lett., 181, 250
Min M., Ormel C. W., Chubb K., Helling C., Kawashima Y., 2020, A&A, 642, A28
Molliére P., Wardenier J. P., van Boekel R., Henning T., Molaverdikhani K., Snellen I. A. G., 2019, A&A, 627, A67
Na C. Y., Esposito L. W., Skinner T. E., 1990, JGR-Atm, 95, 7485
Norwood K., Ng C., 1989, Chem. Phys. Lett., 156, 145
Pacheco-Vazquez S. et al., 2015, A&A, 578 A81
Powell F. X., Lide D. R., 1964, J. Chem. Phys., 41, 1413
Prajapat L., Jagoda P., Lodi L., Gorman M. N., Yurchenko S. N., Tennyson J., 2017, MNRAS, 472, 3648
Rustamkulov Z. et al., 2023, Nature, 614, 659
Saito S., 1970, J. Chem. Phys., 53, 2544
Sarka K., Nanbu S., 2019, J. Phys. Chem. A, 123, 3697
Sauval A. J., Tatum J. B., 1984, ApJS, 56, 193
Setzer K. D., Fink E. H., Ramsay D. A., 1999, J. Mol. Spectrosc., 198, 163
Smith W. H., 1969, J. Quant. Spectrosc. Radiat. Transf., 9, 1191
Stuart B. C., Cameron S. M., Powell H. T., 1992, Chem. Phys. Lett., 191, 273
Stuart B. C., Cameron S. M., Powell H. T., 1994, J. Phys. Chem., 98, 11499
Šurkus A. A., Rakauskas R. J., Bolotin A. B., 1984, Chem. Phys. Lett., 105, 291
Tennyson J., Yurchenko S. N., 2012, MNRAS, 425, 21
Tennyson J., Hulme K., Naim O. K., Yurchenko S. N., 2016, J. Phys. B: At. Mol. Opt. Phys., 49, 044002
Tennyson J. et al., 2020, J. Quant. Spectrosc. Radiat. Transf., 255, 107228
Tennyson J., Furtenbacher T., Yurchenko S. N., Császár A. G., 2023, J. Quant. Spectrosc. Radiat. Transf.
Tiemann E., 1974, J. Mol. Spectrosc., 51, 316
Tiemann E., 1982, J. Mol. Spectrosc., 91, 60
Tsai S.-M. et al., 2023, Nature Astron., 617, 483
Underwood D. S., Tennyson J., Yurchenko S. N., Huang X., Schwenke D. W., Lee T. J., Clausen S., Fateev A., 2016a, MNRAS, 459, 3890
Underwood D. S., Tennyson J., Yurchenko S. N., Clausen S., Fateev A., 2016b, MNRAS, 462, 4300
Vidal T. H. G., Loison J.-C., Jaziri A. Y., Ruaud M., Gratier P., Wakelam V., 2017, MNRAS, 469, 435
Wang H. M., Tang X. S., Han H. Y., Li J. Q., Zhou S. K., Zhang W. J., Chu Y. A., 2005, Chin. J. Chem. Phys., 18, 670
Wang R., Balciunaite U., Chen J., Yuan C., Owens A., Tennyson J., 2023, J. Quant. Spectrosc. Radiat. Transf., 306, 108617
Western C. M., 2017, J. Quant. Spectrosc. Radiat. Transf., 186, 221
Wildt J., Fink E. H., Winter R., Zabel F., 1983, Chem. Phys., 80, 167
Winnewisser M., Gordy W., Sastry K., Cook R. L., 1964, J. Chem. Phys., 41, 1687
Wong M., Amano T., Bernath P., 1982, J. Chem. Phys., 77, 2211
Wu K. T., Morgner H., Yencha A. J., 1982, Chem. Phys., 68, 285
Yamamoto S., 1993, Chem. Phys. Lett., 212, 113
Yamasaki K., Taketani F., Tomita S., Sugiura K., Tokue I., 2003, J. Phys. Chem. A, 107, 2442
Yurchenko S. N., Lodi L., Tennyson J., Stolyarov A. V., 2016, Comput. Phys. Commun., 202, 262
Yurchenko S. N., Sinden F., Lodi L., Hill C., Gorman M. N., Tennyson J., 2018a, MNRAS, 473, 5324
Yurchenko S. N., Al-Refaie A. F., Tennyson J., 2018b, A&A, 614, A131
Yurchenko S. N., Nogué E., Azzam A. A. A., Tennyson J., 2022, MNRAS 520 5183–5191
Zolotov M. Y., Fegley B. J., 1998, Icarus, 132, 431

SUPPORTING INFORMATION

Supplementary data are available at *MNRAS* online.

suppl_data

Please note: Oxford University Press is not responsible for the content or functionality of any supporting materials supplied by the authors. Any queries (other than missing material) should be directed to the corresponding author for the article.

APPENDIX A: THE $b\,^1\Sigma^+ \rightarrow X\,^3\Sigma^-$ BAND, AN EXAMPLE OF INTENSITY CONTRIBUTIONS FROM A FORBIDDEN BAND

Dipole forbidden transitions can arise through multiple mechanisms, such as through the magnetic dipole moment, quadrupole moment, and from intensity stealing. Intensity stealing propagates through the mixture of electronic state wave-functions via couplings such as SOCs and EAMCs, where contributions to the forbidden intensities are derived through taking dipole matrix elements in the eigenstates of the diagonalized Hamiltonian constructed from the coupled $\Lambda - \Sigma$ basis. To understand these intensity contributions to the $X\,^3\Sigma^- \rightarrow b\,^1\Sigma^+$ band, we performed an analysis of the Duo computed electronic state wavefunctions corresponding to the eigensolutions of the diagonalized Hamiltonian which included SOCs, EAMCs, and DMCs for the full 11 state system described in Brady et al. (2022) plus additional $\langle b\,^1\Sigma^+|\mathrm{SO}_x|A\,^3\Pi\rangle$, $\langle a\,^1\Delta|\mathrm{SO}_x|A\,^3\Pi\rangle$ and $\langle b\,^1\Sigma^+|\mathrm{SO}_x|C\,^3\Pi\rangle$ couplings. The contributions to the $X\,^3\Sigma^-$ and $b\,^1\Sigma^+$ computed wavefunctions in the Ω representation are shown in Table A1 which gives the expansion coefficients C_n of the wavefunctions in the eigenbasis of the diagonalized Hamiltonian

$$\Psi_\Omega^{J,\tau} = \sum_n C_n^{J,\tau} |n\rangle, \tag{A1}$$

where J is the rotational quantum number, τ is the parity, and n represents the full set of quantum numbers $|n\rangle = |\mathrm{State}, J, \Omega, \Lambda, S, \Sigma, v\rangle$. We see that because of large SOC between $X\,^3\Sigma^-$ and $b\,^1\Sigma^+$, they share sizeable contributions in their final mixed wavefunctions of their corresponding unmixed basis states. The amount of intensity stealing will then distribute itself through subsequent coupling of the dipole operators in the new mixed-state basis. To this end, we consider the parallel and perpendicular TDMs which couple $\Omega = 0^+ - 0$ and $\Omega = 0^+ - 1$ states, respectively. In spherical tensor form they read, considering the $X\,^3\Sigma^-$ and $b\,^1\Sigma^+$ states,

$$\mu_0 = \left\langle b^1\Sigma_0^+ \middle| \mu_z \middle| X^3\Sigma_0^- \right\rangle, \tag{A2}$$

$$\mu_1 = \pm \left\langle b^1\Sigma_0^+ \middle| 2^{-1/2}(\mu_x \mp i\mu_y) \middle| X^3\Sigma_{\pm 1}^- \right\rangle. \tag{A3}$$

The experimental measurement and analysis by Setzer, Fink & Ramsay (1999) of the $b\,^1\Sigma^+ \rightarrow X\,^3\Sigma^-$ emission band and work by Bernath, Johnson & Liévin (2021) show the μ_0 and $\mu_{\pm 1}$ TDMs

Table A1. The largest expansion coefficients for the $X\,^3\Sigma^-$ and $b\,^1\Sigma^+$ wavefunctions in the Ω representation.

Basis	$\lvert X\,^3\Sigma^-_{0+}\rangle_{\rm DUO}$	$\lvert b\,^1\Sigma^+_0+\rangle_{\rm DUO}$	$\lvert X\,^3\Sigma^-_{+1}\rangle_{\rm DUO}$	$\lvert X\,^3\Sigma^-_{1-}\rangle_{\rm DUO}$
$\lvert X\,^3\Sigma^-_{-1}\rangle$	0	0	0.999 99	0
$\lvert X\,^3\Sigma^-_{+1}\rangle$	0	0	0	0.999 99
$\lvert A\,^3\Pi_{+1}\rangle$	0	0	0	−0.001 19
$\lvert A\,^3\Pi_{-1}\rangle$	0	0	0.001 19	0
$\lvert C\,^3\Pi_{+1}\rangle$	0	0	0	0.000 35
$\lvert C\,^3\Pi_{-1}\rangle$	0	0	−0.000 35	0
$\lvert X\,^3\Sigma^-_{0+}\rangle$	−0.999 64	−0.026 70	0	0
$\lvert b\,^1\Sigma^+_{0+}\rangle$	0.026 69	−0.999 64	0	0
$\lvert A\,^3\Pi_{0+}\rangle$	0.00121	−0.000 93	0	0
$\lvert A\,^3\Pi_{0-}\rangle$	−0.001 21	0.000 93	0	0
$\lvert C\,^3\Pi_{0+}\rangle$	−0.000 34	−0.000 41	0	0
$\lvert C\,^3\Pi_{0-}\rangle$	0.000 00	0.000 40	0	0

Note. The column headers with a subscript 'DUO' are the computed DUO-states which have components in the basis states given as rows due to spin-orbit coupling.

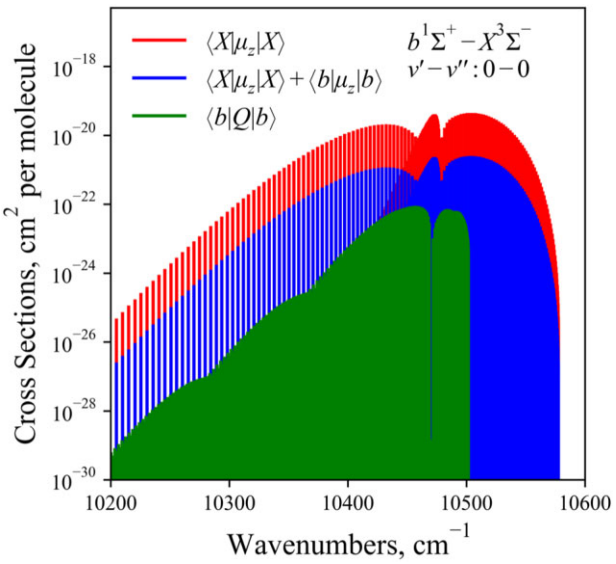

Figure A1. Visualization of the different contributions to the forbidden $X\,^3\Sigma^- \rightarrow b\,^1\Sigma^+$ band intensities. 'Q' refers to the magnetic dipole moment, where the green spectra are due to magnetic dipole transitions, which is orders of magnitude weaker than the intensity stealing mechanism.

to be of the same order of magnitude. However, comparing the $b\,^1\Sigma^+ \rightarrow X\,^3\Sigma^-$ $v = 0 - 0$ band measured by Setzer, Fink & Ramsay (1999) to our semi-empirical line list and the HITRAN empirical line list show disagreements in the P- and R-branch ratios where experiment predicts the P-branch has the most intensity within the band. Considering the intensity stealing mechanism, cross-examining equations (A2) and (A3) with Table A1 reveals that intensity stealing is different for the perpendicular and parallel transitions and therefore the branch ratios for these transitions. This could explain the experimental observation in Setzer, Fink & Ramsay (1999) that the P- and R- branch ratios are different. In an attempt to understand this discrepancy, our analysis on the mixed $X\,^3\Sigma^-$ and $b\,^1\Sigma^+$ state wavefunctions reveals that the competition between the $\langle b\,^1\Sigma^+|\mu_z|b\,^1\Sigma^+\rangle$ and $\langle X\,^3\Sigma^-|\mu_z|X\,^3\Sigma^-\rangle$ DMCs provides the dominant contributions to μ_0, as facilitated through the large $\langle b\,^1\Sigma^+|\mathrm{SO}_z|X\,^3\Sigma^-\rangle$ spin-orbit coupling, where $\langle b\,^1\Sigma^+|\mu_z|b\,^1\Sigma^+\rangle$ subtracts from $\langle X\,^3\Sigma^-|\mu_z|X\,^3\Sigma^-\rangle$ and can be seen in Fig. A1 as the reduction of intensity between the red and blue spectra. μ_1, however, has leading contributions from the $\langle A\,^3\Pi|\mu_x|X\,^3\Sigma^-\rangle$ dipole as facilitated through the $\langle b\,^1\Sigma^+|\mathrm{SO}_x|A\,^3\Pi\rangle$ and $\langle X\,^3\Sigma^-|\mathrm{SO}_x|A\,^3\Pi\rangle$ couplings. We find that the perpendicular TDM μ_1 is responsible for the P–R-branch asymmetry ($P > R$) as seen in the Fourier transform spectroscopy by Setzer, Fink & Ramsay (1999) whereas the parallel TDM μ_0 produces the opposite branch ratios ($P < R$). However, when considering only a vibrationless expansion for our wavefunctions, that is $v = 0$, the μ_1 TDM is very weak producing much lower intensities than the parallel transition moment and as a result the $b\,^1\Sigma^+ \rightarrow X\,^3\Sigma^-$ band has a $P < R$ branch ratio. When considering a larger vibrational basis ($v = 20$) the P–R-branch ratio becomes more sensitive to changes in DMCs and SOCs. From this analysis, we see that the vibrational TDMs have an effect on the rovibrational band intensity distribution in favour of the P–R- branch ratio as seen in Setzer, Fink & Ramsay (1999).

This paper has been typeset from a TEX/LATEX file prepared by the author.